

THESIS FOR THE DEGREE OF LICENTIATE OF ENGINEERING

Electrolyte-Electrode Interfaces in Sodium Metal Batteries

YIHU LI

Department of Physics

CHALMERS UNIVERSITY OF TECHNOLOGY

Gothenburg, Sweden 2025

Electrolyte-Electrode Interfaces in Sodium Metal Batteries

YIHU LI

© YIHU LI, 2025.

Department of Physics
Chalmers University of Technology
SE-412 96 Gothenburg
Sweden
Telephone + 46 (0)31-772 1000

Cover:
[Electrolyte, Na-metal anode, and interphase between]

Chalmers Digitaltryck
Gothenburg, Sweden 2025

Electrolyte-Electrode Interfaces in Sodium Metal Batteries

Yihu Li

Department of Physics

Chalmers University of Technology

Abstract

Sodium metal batteries (SMBs) can achieve high energy densities owing to metal anodes with high specific capacity and low redox potential, and in addition sodium is abundant. Yet, the inherent high chemical and electrochemical reactivity of sodium metal has (so far) limited electrolytes to be created from aprotic solvents (carbonate esters, ethers) because protic solvents dissociate protons via hydrogen bonds and react aggressively. The high reactivity also makes it difficult to correlate electrolyte chemistry with the solid electrolyte interphase (SEI) formation and dissolution, hindering the design of high-performant SMBs.

Herein, we introduce a protic electrolyte based on the N-methylacetamide (NMA) solvent and the NaFSI salt. The coordination of Na^+ and $[\text{FSI}]^-$ to NMA disrupts the hydrogen bonding and strengthens the N-H bond. Optimizing the salt concentration promotes aggregate formation that enhances the SEI stability. We further applied distribution of relaxation times (DRT) analysis to separate the SEI stability and decomposition from other overlapping processes, using more conventional carbonate electrolytes, and could semi-quantify the SEI loss by comparing post-stripping resistances.

Compared to standard organic electrolytes, the optimized NMA formulation produces a chemically distinct, more robust SEI, while the SEI fracture, detachment, and dissolution shows up in conventional carbonate electrolytes when the underlying metal is stripped.

Keywords: Sodium batteries; Sodium metal anode; Electrolyte; Protic solvent; Solid electrolyte interphase; Distribution of relaxation times

List of papers

The thesis is based on the work contained in the following papers:

I Stable interphase enabled use of protic electrolytes in sodium metal batteries

Yihu Li, Tomooki Hosaka, Julia Maibach, and Patrik Johansson

Submitted for publication

II Detection of SEI loss by distribution of relaxation time analysis

Yihu Li, Tomooki Hosaka, Julia Maibach, and Patrik Johansson

In manuscript

Contribution Report

- I YL planned the experiment, and with input from TH, JM, and PJ, performed and analyzed all experiments. YL also wrote the first draft of the manuscript, which was subsequently carefully revised by TH, JM, and PJ.
- II YL planned the experiment in collaboration with TH and PJ and performed and analyzed all experiments with input from TH, JM, and PJ. YL also wrote the first draft of the manuscript, which was subsequently carefully revised by TH, JM, and PJ.

Table of Contents

<i>Abstract</i>	<i>I</i>
<i>List of papers</i>	<i>II</i>
<i>Contribution Report</i>	<i>III</i>
1 Introduction	1
2 Metal batteries	3
2.1 Basic principles of metal batteries	3
2.2 Sodium metal batteries	4
2.2.1 Development overview and challenges	4
2.2.2 Electrolytes	5
2.2.3 Ion transport mechanisms in electrolytes	10
2.3 Electrolyte/electrode interfaces/interphases	11
2.3.1 Formation principles	12
2.3.2 Structure and composition	13
2.3.3 Ion transport across SEI	14
3 Experimental and computational	15
3.1 Electrolyte and electrode preparation, and cell setup	15
3.1.1 Electrolytes	15
3.1.2 Electrode preparation	15
3.1.3 Cell setups	15
3.2 Spectroscopy and microscopy	16
3.2.1 Vibrational spectroscopy	16
3.2.2 X-ray photoelectron spectroscopy (XPS)	18
3.3 Electrochemical characterization	19
3.3.1 Linear sweep voltammetry (LSV)	19
3.3.2 Cyclic voltammetry (CV)	19
3.3.3 Galvanostatic cycling (GC)	20
3.3.4 Electrochemical impedance spectroscopy (EIS) and distribution of relaxation times (DRT)	21
3.3.5 Titration	22
3.4 Molecular dynamics (MD) simulations	22
4 Results and discussion	24
4.1 Electrolyte local structure	24
4.2 SEI formation	27
4.2 SEI dissolution	30
5 Conclusion and outlook	35
<i>Acknowledgements</i>	<i>36</i>
<i>Bibliography</i>	<i>37</i>

1 Introduction

Lithium-ion batteries (LIBs) are today the dominant choice for applications such as electric vehicles and grid storage. However, alternative battery technologies are rapidly advancing. Among them, sodium-ion batteries (SIBs) have gained significant attention due to the natural abundance and low cost of sodium, along with their compatibility with existing LIB manufacturing infrastructure.[1] For instance, hybrid battery packs combining LIB and SIB cells have been developed to extend the range of hybrid electric vehicles.[2]

Despite these advancements, improving the energy density of SIBs remains a key challenge. The current mainstream anode material, hard carbon, suffers from substantial first-cycle irreversible capacity loss, which limits its practical capacity, and it also comes with high production costs.[3] Transitioning to sodium metal anodes, creating a sodium metal battery (SMB), offering a high theoretical capacity of 1166 mAh/g, presents a compelling alternative.[4] However, the high chemical and electrochemical reactivity of sodium metal continues to pose significant challenges in formulating compatible electrolytes. The reduction and decomposition of organic liquid solvents and salt anions in the electrolyte at low potential form a solid electrolyte interphase (SEI) on the sodium metal surface, which in an ideal case should restrain electrolyte decomposition, but to accomplish this is yet a very active R&D area.

Electrolytes for SMBs includes organic solvents,[5] polymers,[6] ionic liquids,[7] and inorganic compounds.[8] Among these, aprotic organic solvent-based liquid electrolytes have traditionally been favoured due to their cost-effectiveness and ease of synthesis. In contrast, protic organic solvent-based liquid electrolytes have received relatively little attention, largely because their O–H and N–H groups can dissociate, releasing protons that readily react with sodium metal.[4, 9] However, Brandt *et al.* demonstrated that in dry protic ionic liquids, the labile proton on the cation is not "free" and the cation is not subject to reversible protonation–deprotonation.[10] This suggests that by carefully controlling proton activity, protic electrolytes could become viable for use in SMBs. Notably, protic solvents are rich in hydrogen bonds (HBs), which can be leveraged to manipulate solvation interactions and stabilize the electrolyte. In such electrolytes, anions from sodium salts can function as HB acceptors, while the protic solvents serve as HB donors. Separately, highly concentrated electrolytes (HCEs) have shown promise in improving stability against sodium metal.[11-12] For example, De Sloovere *et al.* demonstrated that increasing the salt concentration in a mixture of sodium bis(trifluoromethanesulfonyl)imide (NaTFSI) and N-methylacetamide (NMA) reduced

reactivity with sodium metal.[13] Additionally, Na⁺ ions must desolvate before plating, and solvent molecules liberated during desolvation can disrupt the electrode interface, further complicating interfacial stability and influencing subsequent SEI evolution.

The SEI layer formed on a SMB metal anode is ideally strong and intact, but in practice it fractures, cracks and detaches, especially during Na stripping where void formation leads to SEI pitting.[14] Electrochemical impedance spectroscopy (EIS) is a non-destructive *in situ* tool to probe the electrode/electrolyte interface and processes such as ion passage across the SEI, charge transfer at the metal surface, and also mass transport in the bulk electrolyte. A distribution of relaxation time (DRT) analysis can deconvolute an EIS spectrum into peaks, each characterized by a time constant (τ) and associated resistance (R) and capacitance (C).[15] In essence, this technique is sensitive to SEI dissolution. If the SEI partially dissolves during metal stripping, one expects: (1) the SEI impedance/resistance to drop as some insulating layer is removed or thinned; (2) the characteristic τ for Na⁺ transport across SEI to shift to be shorter because of the faster ion transport with a less blocking SEI. And an SEI growth has the opposite effects. For example, Mandl *et al.* found an increase in both τ and resistance of SEI, corresponding to continued SEI formation, even after 25 h at open-circuit voltage (OCV).[16] Increased capacitances obtained from DRT analysis also shows that a more porous SEI exposes more bare sodium metal surface to the electrolyte, whereas a continuous thickening SEI (especially if it is inorganic and dielectric) lowers the capacitance.[17]

The scope of this thesis is to examine how electrolyte chemistry dictates SEI formation, stability, and dissolution on sodium metal anodes. In **Paper I**, using protic NaFSI/NMA electrolytes, we connect proton activity, solvation structure and ion aggregation with interphase properties and evolution using spectroscopic, computational, and electrochemical measurements. In **Paper II**, we analyse quantitative SEI metrics (resistance, capacitance, time constants) to reflect SEI changes by EIS-DRT in commercial carbonate electrolytes during stripping and rest.

2 Metal batteries

2.1 Basic principles of metal batteries

A rechargeable metal battery uses a metal anode paired with a metal-ion-storing cathode material to form an electrochemical energy storage/conversion device. It consists of a cathode, a separator, an electrolyte, a metal anode, and other auxiliary components (Figure 2.1).

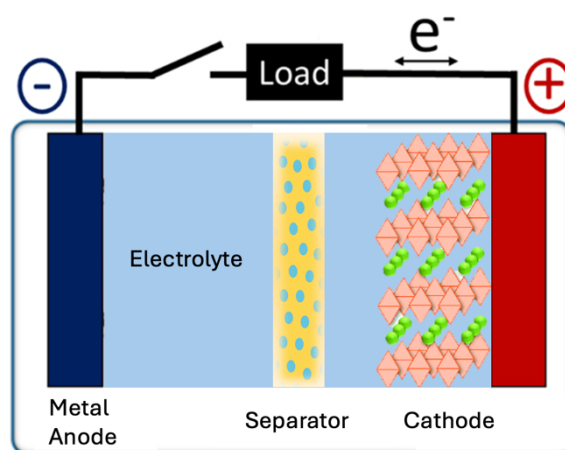


Figure 2.1: Schematic of a metal battery.

During charging and discharging, metal ions shuttle between the cathode and anode, leading to redox reactions at both electrodes.[18] The cathode materials used in metal batteries are similar to those in metal-ion batteries, such as transition metal oxides.[19]

The key difference between a metal-ion “rocking-chair” battery and a metal battery is that metal ions are reduced to metal during charging by electrodeposition and oxidized back to metal ions during discharging, at the metal anode.[20] The former can be split into four steps (Figure 2.2): migration (solvated metal ions migrate across the electrolyte), desolvation (ions remove solvated solvents at the SEI), ion diffusion within the SEI (desolvated ions cross the SEI), and reduction/nucleation (ions gain electrons, deposit as metal, and the deposit grows).[12]

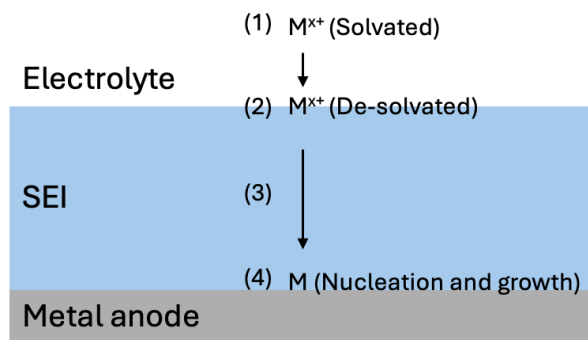


Figure 2.2: Schematic of metal ion electrodeposition at the metal anode.

2.2 Sodium metal batteries

2.2.1 Development overview and challenges

The development of sodium batteries was in parallel with lithium batteries in the 1970s-1980s.[21] A sodium battery prototype, using a sodium-lead alloy anode and a sodium cobalt oxide (NaCoO_2) cathode, was developed jointly by US and Japanese companies, even before the commercialization of LIBs.[22] Although this sodium battery could cycle more than 300 times, its overall performance lagged behind the contemporary LIBs due to a lower operating voltage ($< 3 \text{ V}$) and inherent limitations of sodium ions (Table 2.1);[23] as compared to Li^+ , the larger ionic radius of Na^+ makes it harder to intercalate[24] and its higher density and redox potential further fundamentally result in batteries with lower energy densities than LIBs.

Efforts to enhance energy density led to innovations such as sodium metal-sulfur (Na-S) batteries, which use a liquid sodium anode, a liquid sulfur cathode, and a beta-alumina solid electrolyte with relatively high ionic conductivity (0.1 S cm^{-1}). While these demonstrate promising energy density, they require operational temperatures near 300°C .[25] Maintaining such high temperatures demands external energy input, further complicating their practicality. Coupled with complex system designs, elevated manufacturing costs, and unresolved safety problems, this has constrained the commercial viability of Na-S batteries.[26]

In recent years, room-temperature SMBs have gained significant attention. For example, Chen *et al.* demonstrated a 4.5 V cell at 295 Wh kg^{-1} by forming a robust SEI on the Na anode and cathode electrolyte interphase (CEI) on the $\text{Na}_3\text{V}_2(\text{PO}_4)_2\text{F}_3$ cathode.[27] However, the low first ionization energy of sodium indicates easier electron loss to react with electrolyte.

The high reactivity and low redox potential of sodium metal drives parasitic reactions with most organic electrolytes, forming irreversible SEIs influencing the stripping/plating

behavior.[28] A well-structured SEI could effectively suppress corrosion and guide uniform sodium deposition. On the other hand, a fragile SEI breaks/reforms, consuming both electrolyte and sodium, decreasing the coulombic efficiency (CE) and promoting dendrites, that by easy detachment can be converted into inactive or “dead” sodium.[29]

Table 2.1: Physical and chemical properties of lithium and sodium

Property	Li	Na
Relative Atomic Mass (g mol⁻¹)	6.94	22.99
Electronic Configuration	[He]2s ¹	[Ne]3s ¹
Ionic Radius (nm)	0.076	0.102
Standard Electrode Potential (V)	-3.04	-2.71
Melting Point (°C)	180.5	97.7
Density (g cm⁻³)	0.534	0.968
First Ionization Energy (kJ mol⁻¹)	520.2	495.8
Theoretical Specific Capacity (mAh g⁻¹)	3861	1166
Theoretical Volumetric Capacity (mAh cm⁻³)	2062	1131

2.2.2 Electrolytes

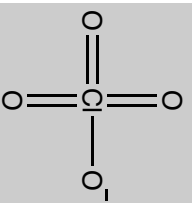
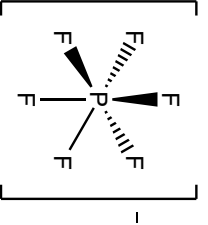
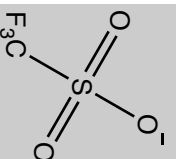
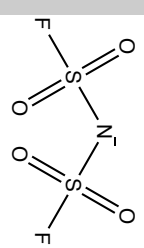
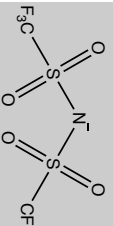
Electrolytes are critical to the operation of batteries, they permeate the cell, wet the cathode, anode, and separator, and serve as the medium for ion transport between electrodes during cycling. An ideal electrolyte must balance multiple properties to ensure good electrochemical performance and safety. High ionic conductivity minimizes resistance and enables rapid ion transfer.[30] A wide electrochemical stability window (ESW) allows the electrolyte to withstand the high voltages required for high energy density batteries.[31] Thermal and chemical stability dictates decomposition under extreme temperatures or reactive conditions, while nonflammability enhances safety.[32]

Composition: Salt(s), Solvent(s), and Additives

An ideal sodium salt should have high solubility and dissociation in the solvents used in order to create plenty of charge carriers, remain stable within the SMB operational voltage range, and be chemically/thermally (meta)stable vs. anode and cathode, to support stable SEI and CEI formation, respectively, for better cycling performance, and inert towards all other battery components.

The salts commonly used are listed in Table 2.2. Thermogravimetric analysis (TGA) shows thermal stability by mass loss to decrease as: $\text{NaClO}_4 > \text{NaTFSI} > \text{NaPF}_6 > \text{NaFSI}$. However, when dissolved to form an electrolyte the order may change, for example in ethylene carbonate/diethyl carbonate (EC/DEC): $\text{NaFSI} > \text{NaTFSI} > \text{NaPF}_6 > \text{NaClO}_4$. [33]

Table 2.2 Properties and advantages/disadvantages of common sodium salts

Name	NaClO ₄	NaPF ₆	NaOTf	NaFSI	NaTFSI
Anion Structure					
Molar Mass (g mol ⁻¹)	122.4	167.9	172.1	203.3	303.1
Melting Point (°C)	474	302	248	122	263
TGA (°C) (%mass loss)	500 (0.09%)	400 (8.14%)		300 (16.15%)	400 (3.21%)
Advantages	Strong oxidative stability; suitable for high-voltage batteries	High solubility/ conductivity in solvents; passivates Al foil; good thermal	Good oxidative/thermal stability	High conductivity; good thermal stability	High conductivity; good thermal/water/oxidative stability
Disadvantages	Explosive in dry state; difficult to remove residual moisture	Poor chemical stability; decomposes into NaF and PF ₅	Forms ion pairs in solvents; low conductivity	Narrow electrochemical window; Al corrosion	Severe Al corrosion

Solvents: An ideal solvent should have a wide electrochemical stability window, high sodium salt solubility, strong dielectric constant, moderate Lewis acidity/basicity, low viscosity, low melting point, high boiling point, and cost-effectiveness. It should remain inert or promote passivation layers during operation, often requiring solvent mixture to balance these properties.

Primary solvent types are mainly esters or ethers. Ester-based solvents (e.g., cyclic carbonates like propylene carbonate (PC) and EC, or linear carbonates like dimethyl carbonate (DMC), DEC, and ethyl methyl carbonate (EMC)) are widely used for their high ionic conductivity and oxidative stability.[34-35] They avoid solvent co-intercalation issues, even in PC-based electrolytes, preventing electrode material exfoliation.[36] Ether-based solvents (e.g., dimethoxyethane (DME), diethylene glycol dimethyl ether (DEGDME), 1,3-dioxolane (DOL), and tetrahydrofuran (THF)) exhibit lower dielectric constants than cyclic carbonates (but higher than linear carbonates). Though prone to decomposition at high voltages, they form thinner SEI layers, enhancing the initial CE.[37]

Additives: Additives, the third major component of electrolytes, are incorporated in small quantities (typically <5%) to address specific shortcomings of the base electrolyte without significantly altering production costs or processes. These components enable targeted enhancements in battery performance, such as stabilizing interfaces, improving safety, or enabling overcharge protection.[38-39]

Film-forming additives are the most extensively studied category. Examples include vinylene carbonate (VC), fluoroethylene carbonate (FEC), sulfur-based additives like 1,3-propane sultone (PST) and 1,3,2-dioxazole thione-2,2-dioxide (DTD), and sodium difluoro(oxalato)borate (NaDFOB).[40-42] These additives are designed to have a narrower ESW than the base electrolyte, allowing them to preferentially oxidize or reduce during initial cycles. This selective reactivity promotes the formation of high-quality SEIs and/or CEIs. For instance, FEC leverages the strong electron-withdrawing effect of F atoms to facilitate stable SEI formation at low potentials, while VC's unsaturated double bonds enable polymerization, creating robust SEI networks.[43]

Flame-retardant additives, such as phosphorus-containing compounds (trimethyl phosphate (TMP), triethyl phosphate (TEP), triphenyl phosphate (TPP)) and fluorinated ethers (e.g., TTE), are critical for reducing electrolyte flammability. These compounds disrupt combustion reactions, enhancing battery safety without compromising electrochemical performance.[44]

Other functional additives include acidity regulators, impurity scavengers and viscosity reducers, each addressing corresponding challenges.[45]

Electrolyte concentration: conventional, highly concentrated, locally highly concentrated and dilute

The electrolyte concentration has historically been 1.0 - 1.2 M, the range that maximizes ionic conductivity (Figure 2.3).[30] This arises from a balance between charge carrier concentration (determined by salt dissociation) and ion mobility (influenced by electrolyte viscosity). While this concentration range is standard for LIBs, it may not be ideal for *e.g.* SMBs.

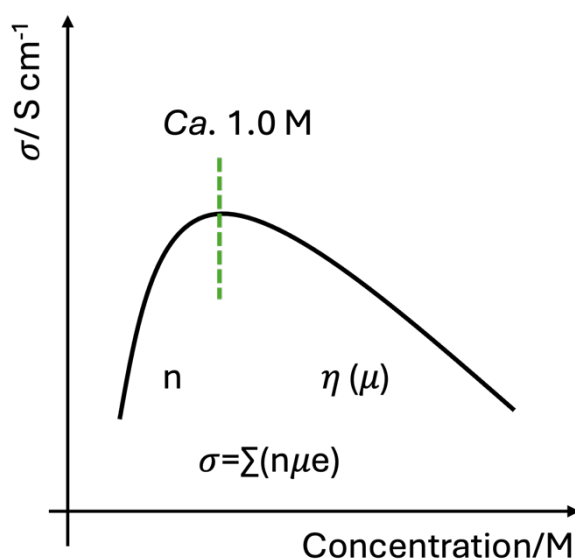


Figure 2.3: The trade-off between charge carrier concentration (n), mobility (μ), and solution viscosity (η) governs the ionic conductivity maximum (σ), typically observed near 1.0 M in LIB non-aqueous electrolytes. Redrawn from [30]

Highly concentrated & locally highly concentrated: Recent advancements in highly concentrated electrolytes (HCEs) offer promising pathways for high-voltage and high energy density batteries. Changing salt concentration significantly impacts solvation structures (*e.g.*, solvent-separated ion pairs (SSIPs), contact ion pairs (CIPs), and ion aggregates (AGGs)) (Figure 2.4), driven by interactions such as cation-anion coulombic forces ($M^+ - X^-$), ion-solvent dipole interactions ($M^+ - \text{solvent}$), and solvent-solvent dipole forces.[46] These structural changes directly influence the redox stability at the electrode interfaces. For instance, a 5 M NaFSI/DME electrolyte mitigates aluminium current collector corrosion by forming a NaF-rich SEI layer in $\text{Na}_3\text{V}_2(\text{PO}_4)_3$ (NVP)/Na cells, enhancing cycling stability and rate

capability.[47] Similar HCEs, such as NaFSI-DEGDME, NaFSI-succinonitrile, NaFSI-DMSO, and NaFSI-TMP, are promising as well.[48-51] However, the high viscosity, sluggish kinetics, and poor wettability toward electrodes and separators make it intrinsically difficult to scale up HCEs. Therefore, a diluent is added to reduce the viscosity, forming localized HCEs (LHCEs). An ideal diluent should exhibit no salt solubility, good miscibility with the main solvent, good electrode compatibility, lower cost than the main solvent, and improved electrolyte safety. For instance, Wang et al. demonstrated a 2.0 M NaFSI/TTE:DME (1:1 mol) LHCE, where the Na^+ solvation structure retained HCE-like anion coordination. This promoted FSI decomposition over DME, generating a dense, NaF-dominated SEI on Na metal anodes.[52] This highlights how altered solvation structures in HCEs/LHCEs can address interfacial challenges.

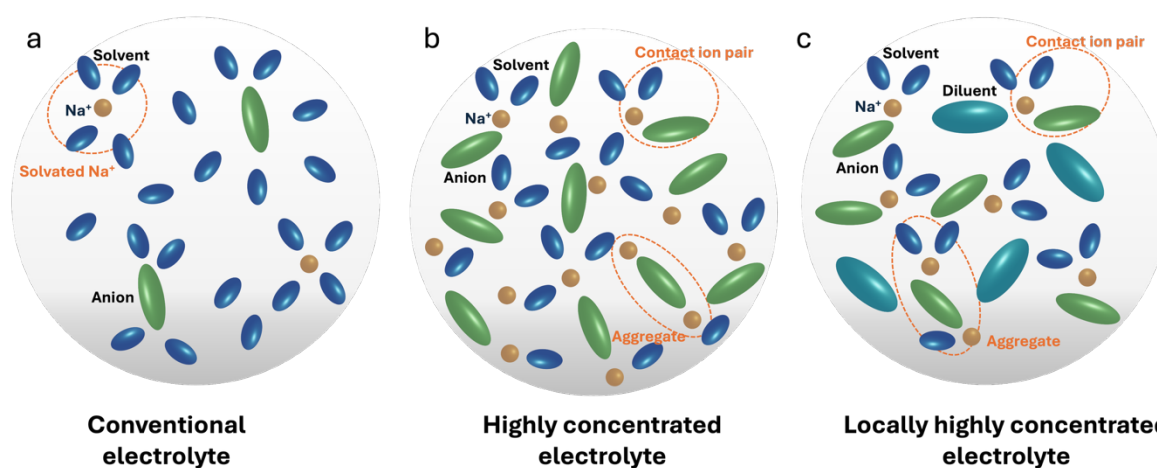


Figure 2.4: From (a) “Conventional” to (b) “Highly concentrated” to (c) “Locally highly concentrated” regime. Redrawn from [46]

Dilute: Moving in the other direction of electrolyte salt concentration is another popular route, this as salts are more expensive than solvents, and thus lowering their content reduces costs. For example, Hu et al. demonstrated use of a dilute electrolyte of 0.3 M NaPF_6 in EC:PC (1:1 vol),[53] while Younesi et al. developed flame-retardant electrolytes: 0.38 M NaBOB in TEP and 0.5 M in TMP, both offering sufficient conductivity ($\sim 5 \text{ mS cm}^{-1}$ at room temperature) and long cycle life in PW//HC cells.[54-55]

2.2.3 Ion transport mechanisms in electrolytes

Ion transport in electrolytes occurs through two primary modes: vehicular and structural.[30] In vehicular transport, ions move with their entire solvation shell.[56] Structural transport, by contrast, involves ions hopping between sites via solvent/anion exchange or dissociation or

large collective motions such as rotations.[30] These mechanisms are not mutually exclusive; ions often exhibit a mix of both, especially as solvation shells quickly reorganize over time.

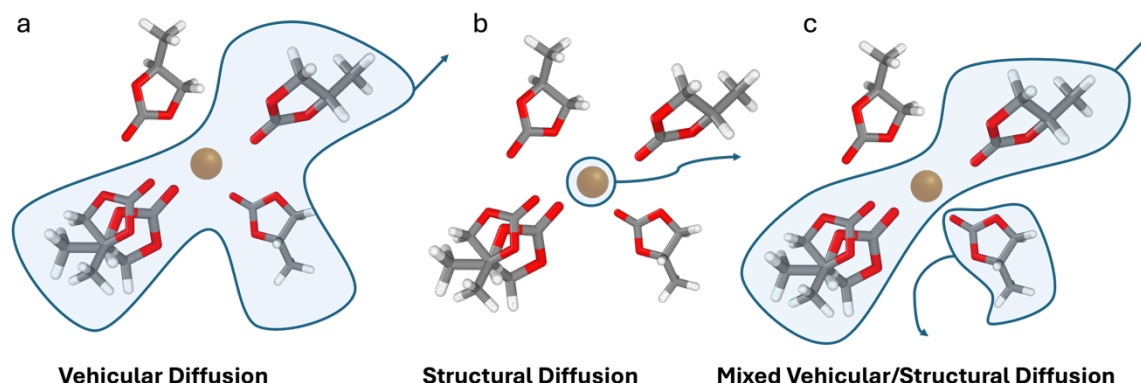


Figure 2.5: Schematic of diffusion mechanisms: (a) vehicular, (b) structural, and (c) hybrid vehicular-structural transport. Redrawn from [30]

The dominance of one mechanism over the other can be quantified and differs between cations; Li^+ in glyme-based electrolytes exhibits strong vehicular behavior due to tight binding with ether oxygen atoms, moving several solvent sizes before exchanging its solvation shell,[56] while Na^+ in similar electrolytes shifts toward structural transport due to weaker ion-solvent interactions.[57-58]

Solvent properties and salt concentration critically influence transport modes. Low-viscosity solvents (e.g., DME, acetonitrile) and small solvents like water favour vehicular motion.[59] However, high salt concentrations often trigger a shift to structural diffusion, as seen in HCEs.[60-61]

Although it is unclear which ion transport mechanism is desirable, structural diffusion may enhance cation transference numbers by decoupling cation and anion motion. The Walden plot, linking molar conductivity and viscosity, helps identify well-dissociated electrolytes, where structural hopping often correlates with improved ion mobility.[62-63]

2.3 Electrolyte/electrode interfaces/interphases

During both resting and initial charge/discharge, interphases, SEIs and CEIs, form at the interfaces that prevent continuous electrolyte decomposition and extends the electrolyte's ESW. The SEIs' and CEIs' density, thickness, and composition significantly influence battery performance. The main research goal is to create a stable protective interphase that enables efficient cation transport. An ideal SEI should: (1) block parasitic reactions through electron

insulation, (2) have high ion conductivity, (3) be stable against electrochemical and thermal degradation, and (4) be mechanically resilient to fracture and dissolution.

2.3.1 Formation principles

Interphase formation is a result of several factors, including the energy mismatch between the electrode and electrolyte, specific adsorption, and ionic solvation.

If the anode's redox potential (μ_A) exceeds the electrolyte's LUMO (lowest unoccupied molecular orbital), electrons spontaneously transfer from the anode to the electrolyte, triggering electrolyte reduction and SEI formation. Conversely, for the CEI, when the cathode's redox potential (μ_C) falls below the electrolyte's HOMO (highest occupied molecular orbital), electrons shift to the cathode, solvent molecules may oxidize (Figure 2.6a).[64] SIB standard carbonate electrolytes are unstable above 4.2 V vs. Na^+/Na .[65]

Specific adsorption precedes solvation, where the inner Helmholtz plane (IHP) is dominated by non-solvated adsorbed species, and the outer Helmholtz plane (OHP) houses solvated ion structures (Figure 2.6b).[66] The initial interfacial composition is thus dictated by adsorbed species, while subsequent interphase growth is further derived by ionic solvation.

Ion solvation structures involve solvated cations and non-solvated anions (Figure 2.6c). Altering ion-ion and ion-solvent interactions change the decomposition; e.g. HCEs with less solvent, lead to more anions to enter the solvation shell, promoting inorganic-rich interphases e.g., NaF, NaCl, Na_2CO_3 .[67]

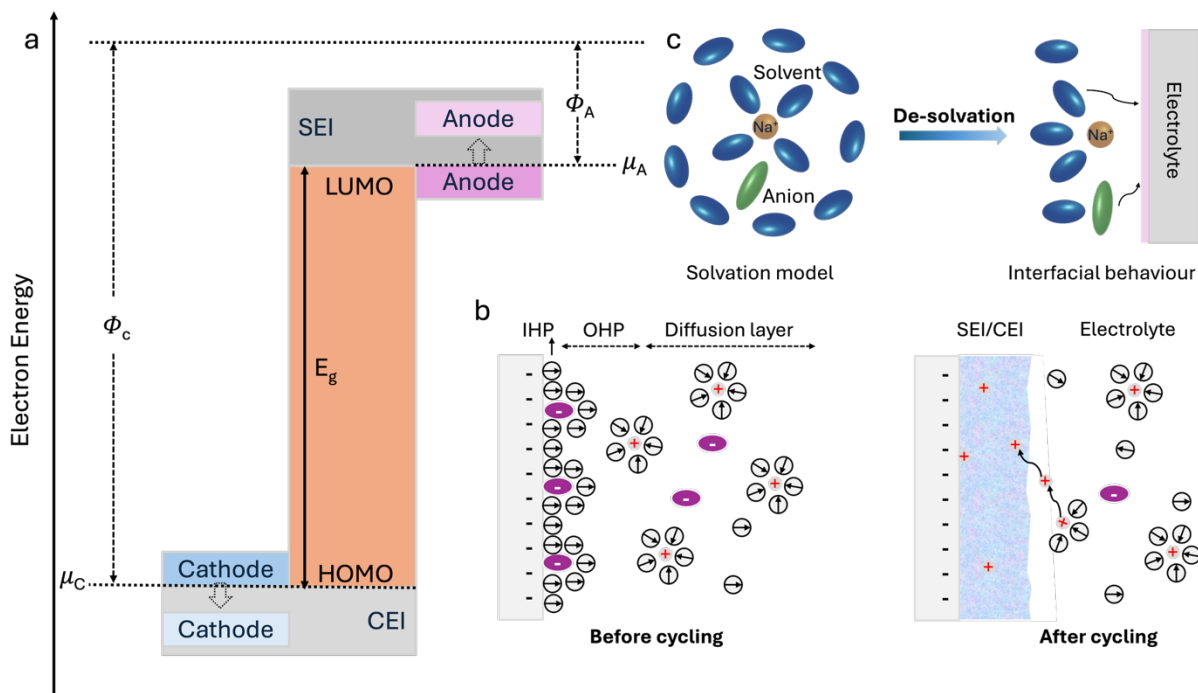


Figure 2.6: (a) Schematic of energy level difference. (b) Schematic of electric double layer (EDL) formation and interphase evolution. (c) Schematic of solvation structure's influence on interphase formation. Redrawn from [66]

2.3.2 Structure and composition

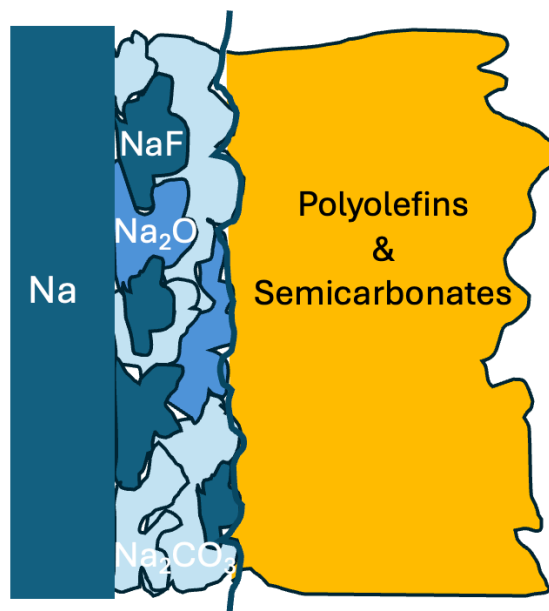


Figure 2.7: Schematic of SEI structure on Na metal.

The SEI composition varies with the depth. It has typically been segmented into an inner inorganic layer and an outer organic layer (Figure 2.7). For SIBs sodium-rich compounds (e.g.,

Na_2CO_3 , Na_2O , NaF , NaCl , Na_2S , Na_2SO_4 , [68] and reduced organic products like ROCO_2Na (R: organic group), [68] respectively.

2.3.3 Ion transport across SEI

The transport of ions across the SEI remains challenging and poorly understood. And there is a paradox; the major ingredients are known as poor ion conductors individually, but for example LIBs can anyhow achieve remarkably high-power densities. This suggests that the SEI components alone cannot explain the conductivity, pointing to alternative ion transport mechanisms.

The "knock-off" mechanism was proposed, with migration enabled by partial coordination with anions during movement. For LIBs this reduces the energy barriers, boosting diffusion. [69] Computational studies further reveal that nanoscale heterogeneity in composite interphases amplifies conductivity, for example interstitials and vacancies create space-charge regions (Figure 2.8) - concentrating charge carriers and increasing mobility by two orders of magnitude vs. the bulk. [70]

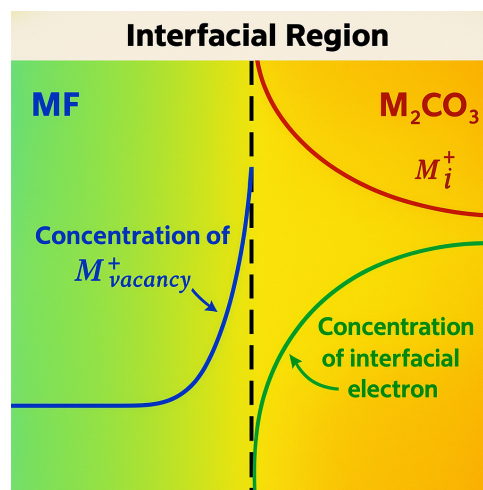


Figure 2.8: MF and M_2CO_3 (M = Li/Na) serve as model interphase components. Redrawn from [70]

3 Experimental and computational

3.1 Electrolyte and electrode preparation, and cell setup

3.1.1 Electrolytes

Our protic electrolytes consist of only NaFSI (Solvionic, 99.9 %) and N-methylacetamide (NMA, Sigma-Aldrich, $\geq 99\%$). NaFSI was pre-dried in a vacuum Büchi oven (< 7 Pa and 24 h at 90°C) and NMA was used as received. Then NaFSI and NMA were mixed at molar ratios of 1.0:0.5, 1.0:1.0, 1.0:1.2, 1.0:1.5, 1.0:2.0, 1.0:3.0, 1.0:4.0, 1.0:5.0, 1.0:7.0, 1.0:8.0, 1.0:9.0, 1.0:10.0, 1.0:20.0 and 1.0:30.0 under heating at 80°C .

Benchmarking electrolytes: 1.0 M NaPF_6 in EC:PC (50:50 w/w) was purchased from E-lyte, 1.0 M LiPF_6 in EC:DEC (50:50 v/v) from Sigma-Aldrich and 1.0 M NaPF_6 in EC:DMC (50:50 v/v) w/o 5% FEC from DoDoChem (H_2O : 20 ppm max).

3.1.2 Electrode preparation

The copper /aluminium foil and sodium metal were purchased from Goodfellow and Aotelec. NVP as the cathode was prepared by making a slurry consisting of NVP, Super P (MTI), and poly (vinylidene fluoride) ((PVdF), Sigma Aldrich) in a weight ratio of 80:10:10 in N-methyl pyrrolidone (NMP, Sigma Aldrich). The slurry was then coated onto an Al foil using an automatic coater and dried overnight at 80°C under vacuum. The mass loading in the NVP electrode was approximately $4 - 5 \text{ mg cm}^{-2}$.

3.1.3 Cell setups

R2032 coin cells were used for electrochemical performance tests with working electrodes (WEs) selected from NVP cathode, Cu, Al, and Na based on test purposes (Figure 3.1). All coin cells used glass fibre separators and Na foil as counter electrode.

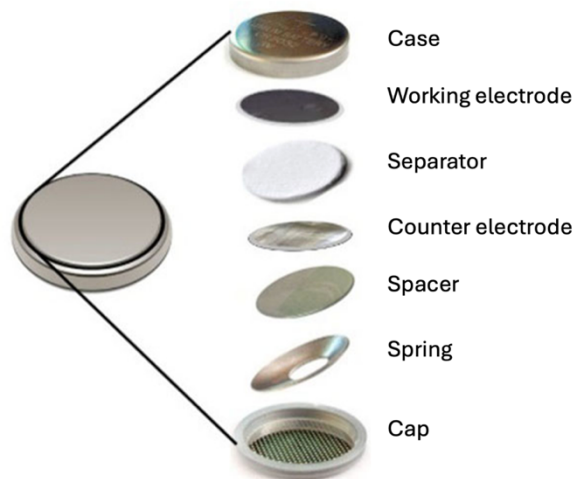


Figure 3.1: Coin cell parts.

A 3-electrode cell configuration is essential to isolate influences of counter electrode during measurement, particularly crucial for SEI investigation on WEs. Also maintaining constant pressure governs the SEI reproducibility. Therefore, PAT cell setup was purchased from EL-Cell for characterizing SEI dissolution (Figure 3.2). Insulation sleeve (PP) with reference electrode of Na ring and GF/A separator (glass fiber, 260 μm) was used for this cell setup.

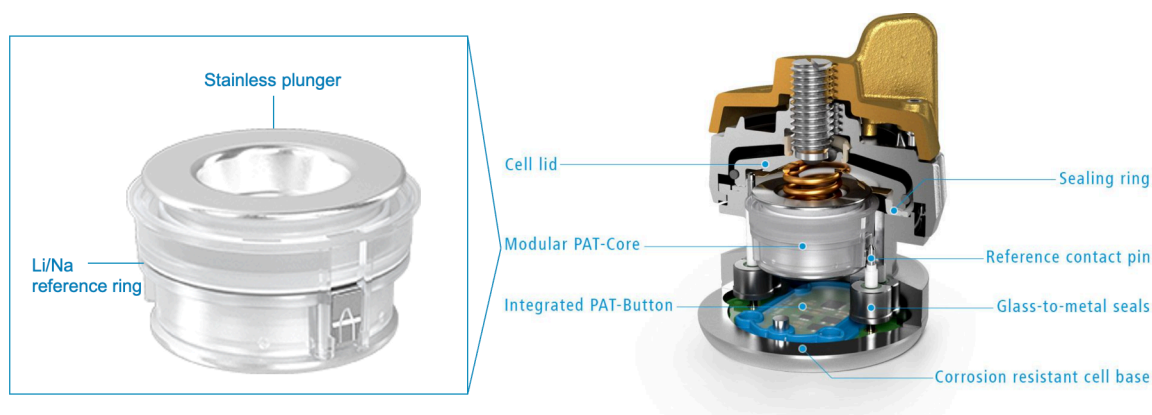


Figure 3.2: PAT cell parts.

3.2 Spectroscopy and microscopy

3.2.1 Vibrational spectroscopy

Raman spectroscopy

Raman spectroscopy is a technique originating from transitions in vibrational and rotational energy levels and depends on the changes in the polarizability during excitation. By correlating vibrational mode frequencies, intensities and their changes, we can obtain local structural information, such as ion-ion and ion-solvent interactions.[71]

The base is that as monochromatic radiation passes through a transparent substance, some is scattered (Figure 3.3). Most of the scattered radiation's frequency is the same as the incident radiation. This is Rayleigh scattering. Some scattered radiation has lower or higher frequencies; Raman scattering, Stokes and anti-Stokes. A complication is that this mechanism overlaps with excessive energy lost as heat through vibrational relaxations, followed by returning to the ground state and emitting a photon of lower energy than absorbed light, i.e. fluorescence.[72]

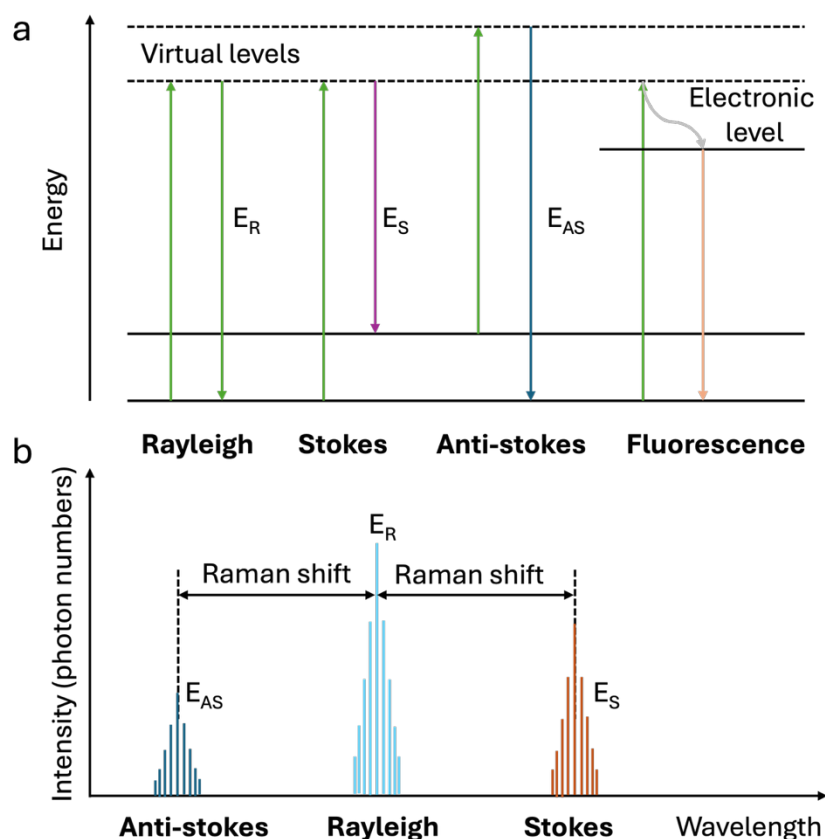


Figure 3.3: (a) Energy diagrams of Rayleigh, Stokes, anti-Stokes scattering, and fluorescence and (b) their Raman spectrum. Redrawn from [72]

In this thesis, the presence of $[FSI]^-$ is observed using Raman shifts ranging from 700 cm^{-1} to 790 cm^{-1} . This corresponds to the S-N-S bending mode of $[FSI]^-$. NMA solvent and protic electrolytes were studied using a Bruker MultiRAM FT-Raman spectrometer, having a spectral resolution of 2 cm^{-1} and a Nd:YAG laser (1064 nm , 300 mW) as the excitation source. The results were averaged across 2000 scans. The data for the electrolytes, placed in glass vials, were collected at room temperature. Gaussian-shaped peaks were used for the peak fitting.

Fourier-transform infrared (FTIR) spectroscopy

Infrared spectroscopy is similar to Raman spectroscopy but uses infrared radiation which a molecule absorbs only selected frequencies (energies) of, those matching its natural vibrational frequencies having a dipole moment that changes.[73]

In this thesis, the N-H stretching mode of NMA is of interest with a typical range from 3100 cm^{-1} to 3500 cm^{-1} . We used a Bruker Alpha ATR-FTIR spectrometer and a diamond crystal to study the single NMA solvent and all the protic electrolytes. For each sample, 64 scans with a resolution of 2 cm^{-1} were made.

3.2.2 X-ray photoelectron spectroscopy (XPS)

XPS is a widely used surface analysis technique. It reveals chemical state information via an x-ray of a fixed energy ($h\nu$) irradiating the sample, and the x-ray energy is transferred to a core level electron to make it emit to the vacuum level. The kinetic energy (E_K) of the emitted electron is measured by an electron analyzer to be used to calculate binding energy (E_B , BE) according to equation 3-1, where is Φ the spectrometer work function.[74]

$$h\nu = E_B + E_K + \Phi \quad (3-1)$$

The sensitivity of XPS lies in those electrons close to the sample surface that are able to easily escape out to the analyzer. The escape probability for electrons tends to decrease exponentially with greater depth. The depth that XPS can reach is different and dependent on the material density, molecular weight, band gap energy and number of valence electrons. One can use sputter-etching for depth profiling but should pay attention to the potential damage on the sample by high-energy and long-lasting x rays.[74]

In this thesis, we performed XPS measurement using a PHI5000 Versa Probe III spectrometer with a monochromated Al $K\alpha$ source (1486.6 eV, 100 μm spot). Samples were washed with dimethyl carbonate (DMC, Sigma-Aldrich, anhydrous, $\geq 99\%$) and vacuum-dried. Spectra were acquired at 0.1 eV step size and 55 eV pass energy, processed via CasaXPS. C1s hydrocarbon (284.8 eV) was the energy reference, with ± 0.1 eV binding energy uncertainty and ± 0.05 eV full width at half maximum (FWHM). Shirley background and Voigt profiles (70% Gaussian, 30% Lorentzian) were applied; no normalization. Survey spectra identified elements (atomic ratios via sensitivity factors): C (0.296), O (0.711), Na (1.685), F (1.000), S (0.570), N (0.477), Ca (1.634, impurity).[75]

3.3 Electrochemical characterization

3.3.1 Linear sweep voltammetry (LSV)

In LSV, the voltage is scanned from a lower limit to an upper limit (Figure 3.4a), with the current response as a function of voltage (Figure 3.4b). Initially, the current increases as there are enough reactants near the electrode surface, and the diffusion layer allows for fast transport of reactants from the electrolyte bulk. However, this current peak is reached when reactants near the electrode have been consumed enough to create a thick diffusion layer. This leads to insufficient replenishment of reactants from the bulk, resulting in a decreasing current. Besides, increasing the scan rate increases the current response as well.[76]

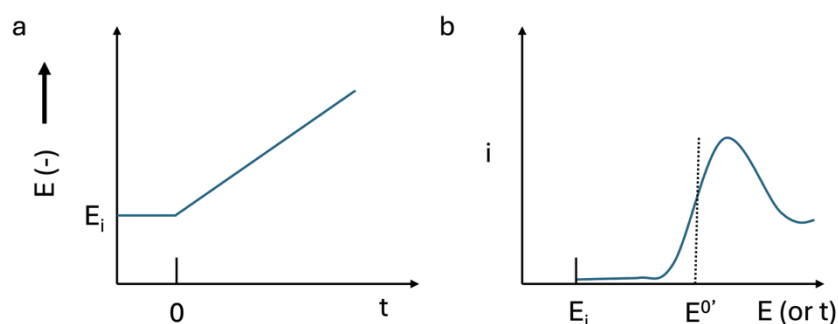


Figure 3.4: (a) Linear voltage sweep and (b) resulting current response.

In this thesis, LSV curves were acquired in Na//Cu and Na//Al with a scan rate of 1.0 mV s^{-1} to investigate the electrochemical stability window of prepared protic electrolytes.

3.3.2 Cyclic voltammetry (CV)

CV is similar to LSV, but the voltage scan is reversed to the lower limit after reaching the upper limit at a fixed rate (Figure 3.5). A reversible electrochemical reaction recorded by CV has the following characteristics: (1) The voltage separation between the current peaks is $\Delta E = E_p^a - E_p^c = \frac{59}{n} \text{ mV}$, where n is the number of electrons transferred in a redox reaction; (2) The positions of peak voltage is independent of the scan rates; (3) The ratio of the peak currents is equal to one; (4) The peak currents are proportional to the square root of the scan rate.[76]

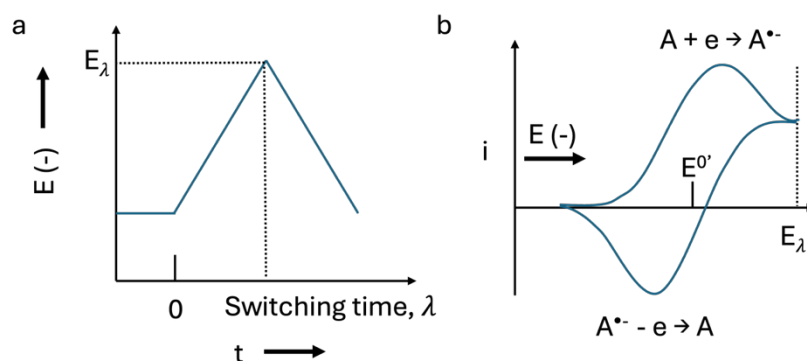


Figure 3.5: (a) Cyclic potential sweep, (b) Resulting current response.

In this thesis, CV curve tests were performed in Na//Cu from -1.0 and 2.0 V vs. Na^+/Na at a sweep rate of 1.0 mV s^{-1} to evaluate the reversibility of Na plating/stripping in prepared protic electrolytes.

3.3.3 Galvanostatic cycling (GC)

GC is an electrochemical testing method to understand reaction mechanism and evaluate battery performance by repeatedly charging and discharging under constant current conditions.

In this thesis, as for the SEI stability test, we first cycled the Na//Cu cells between 0.005 V and 2.0 V vs Na^+/Na for five cycles to form the SEI, followed by a 50-hour pause before resuming the next cycle. If the SEI dissolves during the pause, the reduction capacity in the next cycle will compensate for the SEI loss. By comparing the reduction capacity before and after the pause, we could calculate the extent of SEI dissolution.

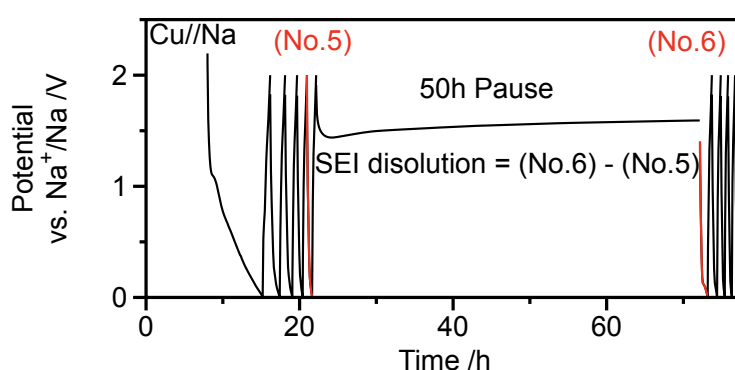


Figure 3.6: Galvanostatic cycling procedure.

3.3.4 Electrochemical impedance spectroscopy (EIS) and distribution of relaxation times (DRT)

EIS is a non-destructive technique to diagnose batteries. It applies a small perturbation, a sinusoidal signal (ac voltage or ac current) over a wide range of frequencies, to an electrochemical cell in equilibrium and monitors the sinusoidal response (current or voltage) toward the applied perturbation. During measurement, linearity, causality and stability should be achieved. EIS can measure different processes, but they may be convoluted together. Experience-dependent equivalent circuit model (ECM) cannot guarantee accurate interpretation of electrochemical processes, as a single EIS spectrum may fit multiple models. The DRT method addresses this by translating frequency-domain data into time constants, directly isolating dominant processes (Figure 3.7). This avoids ECM assumptions, simplifying analysis and improving accuracy.[15]

Each process, such as electrolyte resistance, bulk vs. grain boundary conductivity in polycrystalline solids, electric double-layer charging/discharging, charge-transfer reaction kinetics, and mass transport, has a unique time constant ($\tau = RC$), where R is resistance and C is capacitance. To calculate the polarization resistance of a specific process from a DRT curve, corresponding DRT peak needs to be integrated over its relaxation-time range. In continuous form, for a process spanning from $\ln\tau_1$ to $\ln\tau_2$: $R_{process} = \int_{\ln\tau_2}^{\ln\tau_1} \gamma(\ln\tau)d(\ln\tau)$, which produces a value in ohms.

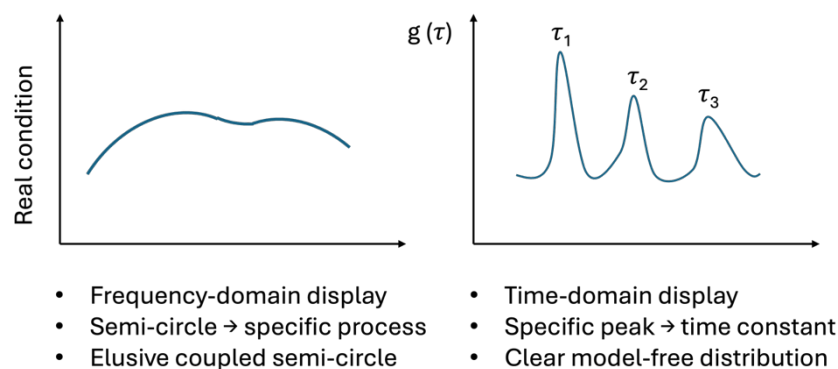


Figure 3.7: EIS based Nyquist plots and resulting DRT curve. Redrawn from [15]

In this thesis, to study SEI formation in protic electrolytes, we obtained EIS data of the Na//Cu cell at a frequency region of 10 Hz to 10^5 Hz. Two EIS measurements were taken at 5 minutes and 45 minutes after plating 10 μ Ah of Na onto Cu. As for studying SEI dissolution, EIS measurements for both Na//Cu and Na//Na cells were conducted in the frequency range of 10

Hz to 10^5 Hz. After an eight-hour rest, initial EIS measurements were taken. Sodium (2 mAh cm^{-2}) was then plated at 1 mA cm^{-2} onto WE, rested for 5 hours, and EIS was measured again. After stripping 0.05 mAh cm^{-2} of sodium at 10 mA cm^{-2} in the following steps, each stripping step was followed by a 5-hour rest, and EIS measurements were taken after each rest. DRT analysis for all of the EIS data was conducted using pyDRTtools.[77] The regularization parameter was calculated by using generalized cross-validation (GCV).[78]

3.3.5 Titration

Titration is a quantitative laboratory technique used to determine the concentration of a known analyte. A standardized solution of precisely known concentration, called the titrant, is gradually added to react with the analyte. By measuring the titrant's volume required for a complete reaction, the analyte's concentration is calculated.

In this thesis, titration tests were conducted in Na//Cu cells to quantify SEI growth. During each titration step, $10 \text{ } \mu\text{Ah}$ of sodium (titrant) was plated onto copper at 0.05 mA cm^{-2} , followed by an open-circuit potential (OCP) relaxation phase at $\sim 0 \text{ V}$ (enabled by sodium presence on both electrodes). The OCP phase ended when the voltage exceeded 0.05 V , signalling full titrant consumption (Figure 3.8). This cycle, plating, relaxation, and voltage threshold termination was repeated for 10 times in this study to track SEI dynamics.

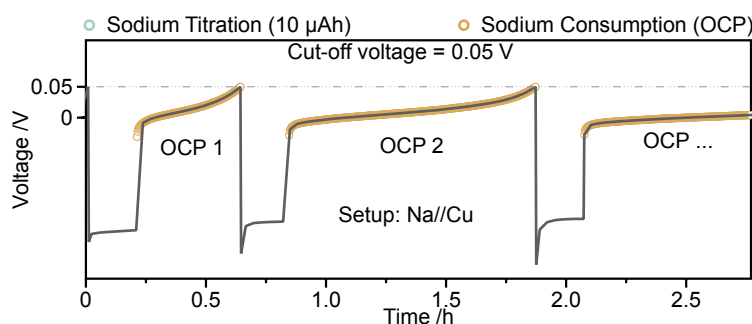


Figure 3.8: Coulombic titration procedure.

3.4 Molecular dynamics (MD) simulations

MD simulations track and analyse atomic and molecular motions using Newtonian mechanics, with interatomic forces derived from the gradient of a potential energy surface. By resolving these interactions, MD provides critical insights to elucidating electrolyte structures and behaviour.[79]

In this thesis, we performed MD using GROMACS with the non-polarizable OPLS-AA force field.[80-82] First, the electrolyte of interest was placed in a cubic simulation box measuring

70×70×70 Å³ with the initial configuration created using the Packmol software.[83] Energy minimization was then carried out to remove unfavourable contacts and achieve a local minimum. The electrolyte then underwent 4 ns of isothermal-isobaric ensemble (NPT) equilibration using a Berendsen barostat set to 1.01325×10⁵ Pa and a V-rescale thermostat at 298.15 K. Next, a 2 ns canonical ensemble (NVT) equilibration phase was performed at the same temperature, maintained by the V-rescale thermostat.[84] Production MD runs of 60 ns followed, employing a time step of 2 fs and the Particle-Mesh Ewald (PME) method to handle long-range electrostatic interactions. Hydrogen bonds were counted with distance cutoff of 0.35 nm and angle cutoff of 30°.[85]

4 Results and discussion

This section centers on the overarching research question: "How do electrolyte formulations—from unconventional protic electrolytes to commercial formulations—influence the formation, stability, and dissolution of the SEI?" We start by studying the local structure of formulated high-concentration electrolytes, i.e., increasing the NaFSI:NMA ratio, using Raman spectroscopy, FTIR spectroscopy and MD simulation in section 4.1. Subsequently, we assess the impact of the electrolyte composition on the SEI formation through Coulometric titration and XPS in section 4.2. Finally, we characterize the SEI stability vs. dissolution during rest and further quantitatively estimate SEI dissolution triggered by metal using DRT in section 4.3.

4.1 Electrolyte local structure

Raman spectroscopy reveals that the peak corresponding to the S-N-S bending mode of $[\text{FSI}]^-$ progressively moves to higher Raman shifts as the concentration of NaFSI increases from NaFSI:NMA=1:30 to 1:0.5 (Figure 4.1a).[86-87] This movement indicates stronger interactions between $[\text{FSI}]^-$ and Na^+ , forming ion pairs and even aggregated ion clusters. Specifically, at $\approx 726 \text{ cm}^{-1}$, a peak observed at the most dilute ratio of NaFSI:NMA=1:30 represents the free $[\text{FSI}]^-$ that is not corradated to Na^+ , suggesting that the Na^+ is largely solvated by NMA. With less NMA (1:1.5, 1:1.2 and 1:1.0), both contact ion pairs (CIP), at ca. $736\text{-}737 \text{ cm}^{-1}$ and aggregates at ca. $746\text{-}755 \text{ cm}^{-1}$ are the main electrolyte constituents. The peak percentages for each species show that CIP declines from ca. 30% to ca. 19%, whereas both AGG-I and AGG-II increase by ca. 5-10% each (Figure 4.1b). MD simulation further corroborates the aggregates formation is a function of salt concentration, by showing an increased partial coordination number (pCN) of Na- O_{FSI} (Figure 4.1c). In NMA, the carbonyl (C=O) group and the adjacent nitrogen atom are connected through a partial double bond due to resonance. This resonance involves the delocalization of the lone pair of electrons on the nitrogen atom into the carbonyl group,[88-89] creating a conjugated system that enables O_{NMA} to coordinate with Na^+ as well. Nevertheless, as the concentration of NaFSI rises, fewer NMA present in the solvation sheath of Na^+ , as indicated by a decreasing Na- O_{NMA} pCN when the electrolyte ratio shifts from NaFSI:NMA =1:1.5 to 1:1.0 (Figure 4.1d). As a result, the aggregates that form may induce anion-derived SEI with enhanced stability.[11]

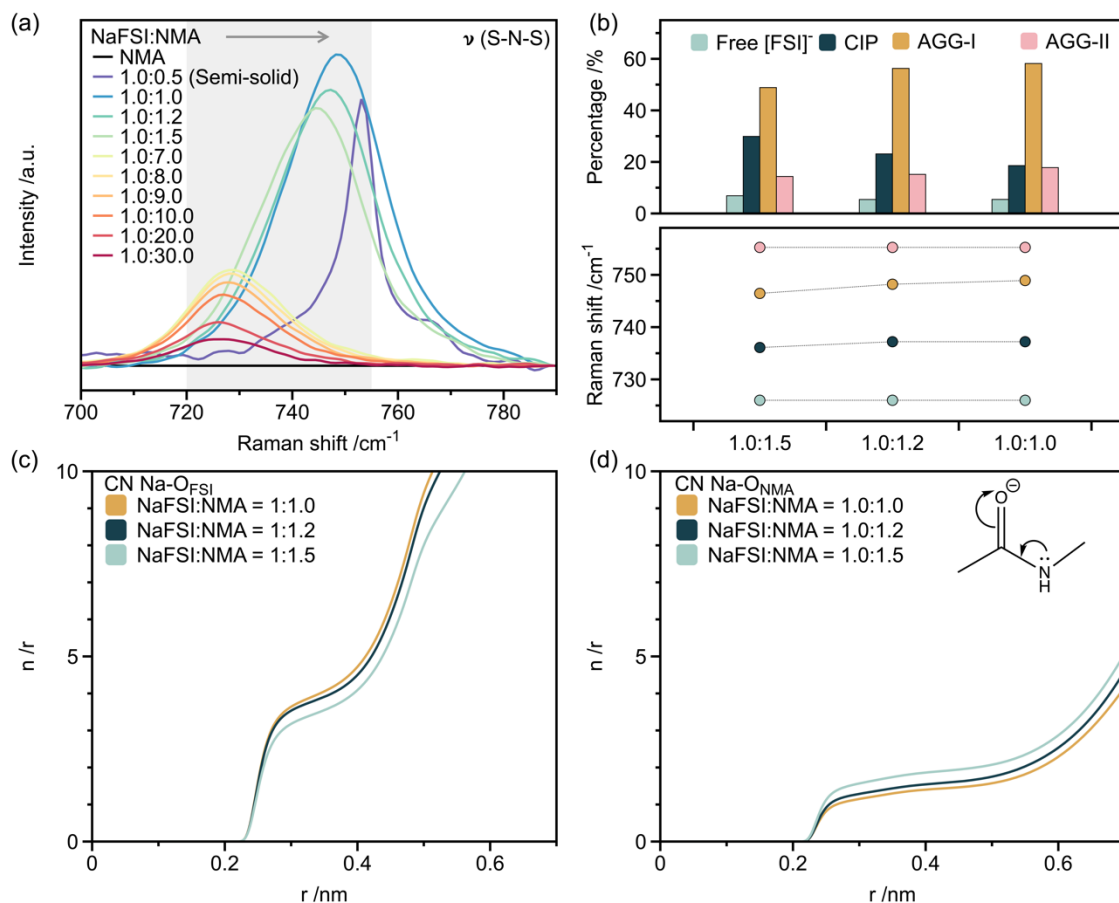


Figure 4.1: (a) Raman spectra in the region of the peak of the S-N-S bending mode of [FSI]⁻, (b) speciation and Raman shifts of “free” [FSI]⁻, CIPs, AGG-I and AGG-II. pCNs from MD simulation: (c) Na-O_{FSI} and (d) Na-O_{NMA} vs. distance (r). All as function of salt concentration.

FTIR spectra complement these findings. In pure NMA, the H-bonded N-H stretching mode is observed at *ca.* 3290 cm⁻¹,^[90] whereas in the electrolytes a new non-H-bonded N-H peak appears at *ca.* 3425 cm⁻¹ (Figure 4.2). Both display blue shifts with increasing salt concentration, which suggests a shortening or strengthening of the N-H bond.^[91-92] This effect most likely arises because Na⁺ preferentially interacts with O_{NMA}, thereby competing with and partially disrupting the intra- and intermolecular HB network among NMA molecules.

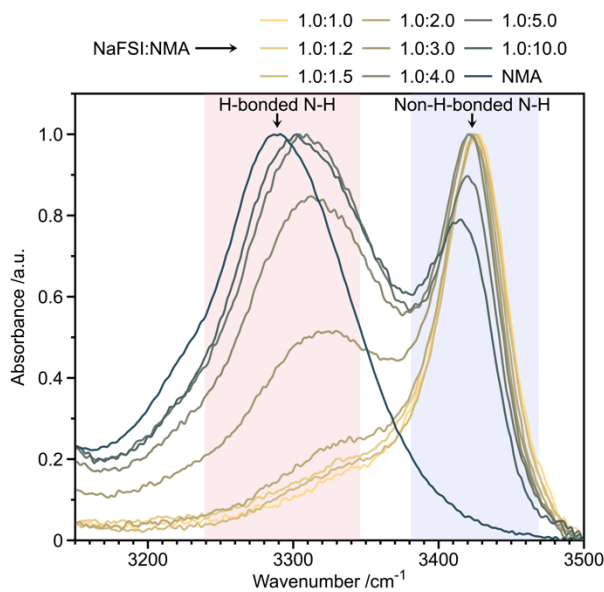


Figure 4.2: FTIR spectra of the N-H stretching mode peak of NMA as function of salt concentration and for pure NMA

The reduction in the number of HBs per H_{NMA} is evident in Figure 4.3a, reducing the likelihood of proton dissociation that reacts with Na metal. Although also O_{FSI} can interact with $N\text{-}H_{\text{NMA}}$,^[93] potentially weakening the N-H bond, its effect is minimized because the electronegativity of O_{FSI} is largely neutralized by Na^+ in HCEs. Combined with steric hindrances, this collectively results in weaker and fewer interactions between $N\text{-}H_{\text{NMA}}$ and O_{FSI} ; with $H_{\text{NMA}}\text{-}O_{\text{FSI}}$ distance longer than $H_{\text{NMA}}\text{-}O_{\text{NMA}}$ (Figure 4.3b), on average only *ca.* 0.5 O_{FSI} and almost no F_{FSI} drag H from $N\text{-}H_{\text{NMA}}$ (Figure 4.3c-d). Therefore, the net result is a strengthened N-H bond as salt concentration increases.

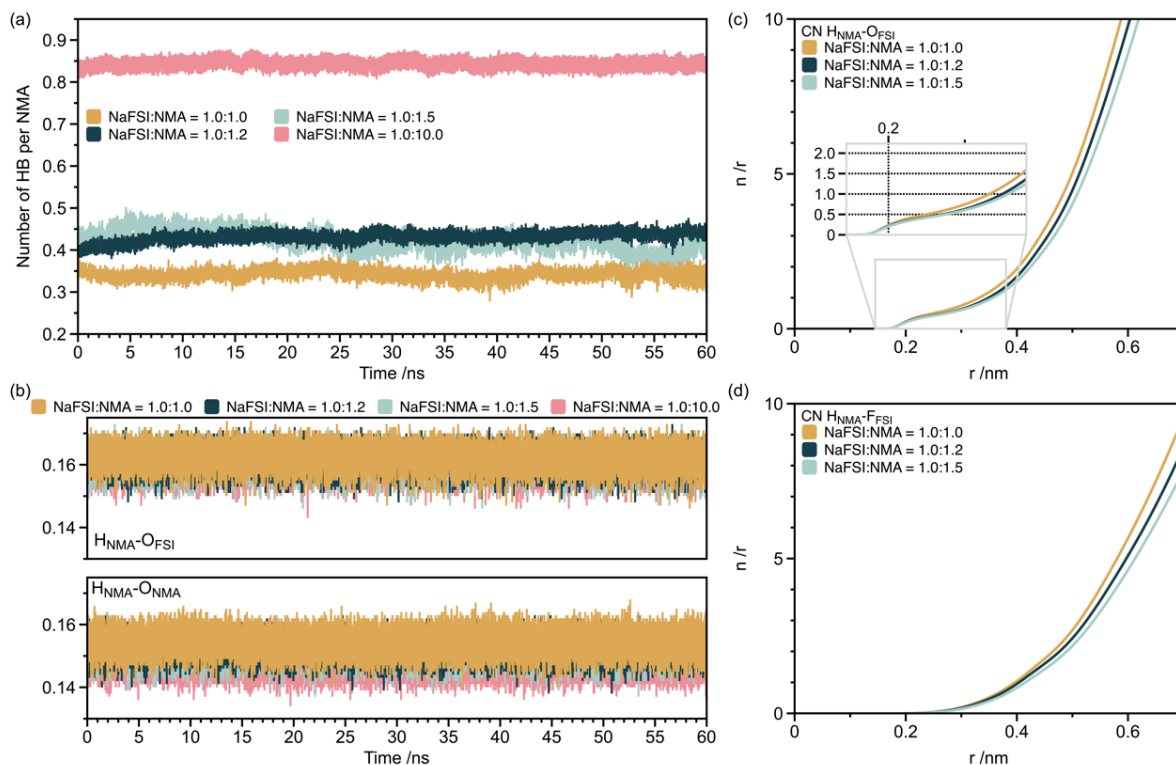


Figure 4.3: (a) Number of intramolecular and intermolecular hydrogen bonds per NMA, and (b) minimum HB distance between $H_{\text{NMA}}\text{-O}_{\text{FSI}}$ and $H_{\text{NMA}}\text{-O}_{\text{NMA}}$; Partial coordination number for (c) $H_{\text{NMA}}\text{-O}_{\text{FSI}}$ and (d) $H_{\text{NMA}}\text{-F}_{\text{FSI}}$.

4.2 SEI formation

Coulometric titration demonstrates SEI passivation by showing that, after the initial formation of a passivation layer, the kinetics of sodium titrant consumption slows down significantly. [94] This test turns the stability between electrolyte and Na metal anode into a measurable time. Vigorous side reactions cause all electrolytes to quickly consume *ca.* 10 μAh of titrant at the initial cycle. With passivation layer formed to inhibit side reactions, longer times are required in the following cycles (Figure 4.4a). Notably, the rate of the open circuit potential (OCP) increase varies among electrolytes, reflecting their different SEI passivating ability. As the electrolyte salt concentration increases from NaFSI:NMA=1.0:1.5 to 1.0:1.0, the SEI passivation improves, evidenced by the longer OCP time needed to deplete the sodium titrant. This observation aligns well with the results of Raman and FTIR spectroscopy data as well as the MD simulation: a higher salt concentration promotes aggregate formation and stronger N–H bonds in NMA, which likely enhances SEI formation and stability.[13] Benchmarking with a commercial aprotic organic liquid electrolyte, 1.0 M NaPF₆ in EC:PC (50:50 w/w), shows

that only the NaFSI:NMA=1.0:1.0 electrolyte has a superior passivation across all titration cycles. After the sixth titration, the OCP time of the benchmark electrolyte levels off, attributing the most stable and complete interphase achievable with this electrolyte. By using linear sweep voltammetry (LSV) we confirm that the NaFSI:NMA=1.0:1.0 electrolyte has the best reductive stability (Figure 4.4b).

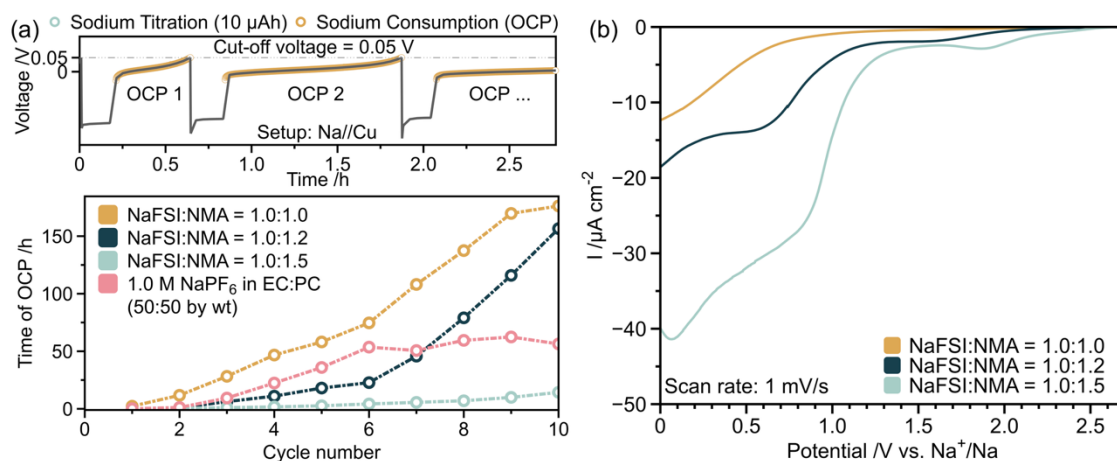


Figure 4.4: (a) Coulometric titration time required to exhaust a Na titrant of 10 μAh , and (b) reductive stability of the electrolytes.

XPS results show little difference in surface composition with changing electrolyte salt concentration (Figure 4.5a), while larger C contributions and smaller Na, F, S, and N contributions (Table 4.1) are observed as salt concentration increases, even though a salt-derived SEI is expected.[11-12, 95]

We attribute the largest C contribution of the C1s spectra to Na₂CO₃ (Figure 4.5b), which becomes increasingly prominent with electrolyte salt concentration increasing (Figure 4.5c and Table 1). Thus, this C contribution is not an organic one, but an inorganic, as initially expected. In addition, the NS=O signals in the N1s spectra from [FSI]⁻ suggest a more inorganic-rich SEI. The reduced C–N intensities from NMA in the N1s spectra (Figure 4.5d and Table 1) indicate less NMA decomposition. Since NMA is the sole carbon source, the growing C contribution as salt concentrations increases must instead derive from the native carbonate layer on pristine Na, detectable when the SEI is sufficiently thin. Therefore, the higher carbon content does not imply increased NMA degradation or a more organic SEI.

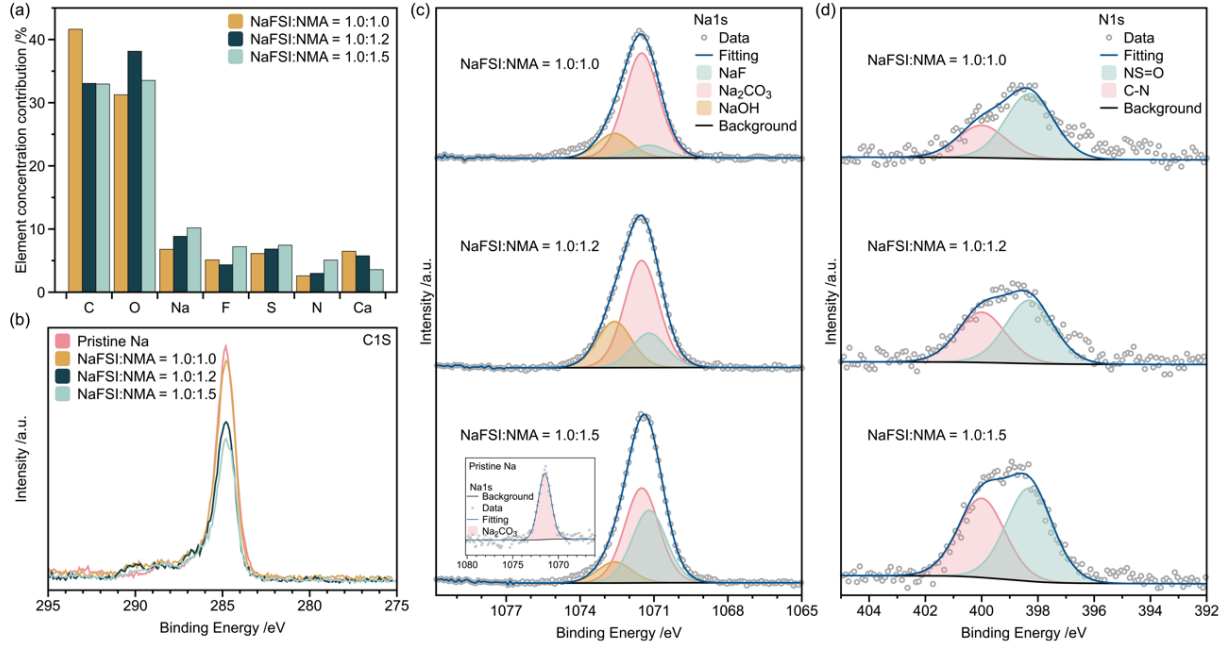


Figure 4.5: (a) Relative element concentration contributions to the XPS spectra from Na electrode surfaces after two full cycles in Na/Na₃V₂(PO₄)₃ cells at 0.1 C rate, (b) C1s spectra before and after two cycles, and (c) Na1s and (d) N1s spectra (after two cycles), respectively, using the different electrolytes.

Table 4.1: Relative contributions of species to the Na1s and N1s spectra.

NaFSI:NMA ratio	Na1s spectra assignments and relative contributions			N1s spectra assignments and relative contributions	
	Na ₂ CO ₃ [75]	NaF[96]	NaOH[97]	C-N[98-99]	NS=O[100]
	1071.50 eV	1071.20 eV	1072.60 eV	400.00 eV	398.30 eV
1.0:1.5	50%	39%	11%	46%	54%
1.0:1.2	57%	18%	25%	44%	56%
1.0:1.0	74%	17%	9%	33%	67%

Moreover, cyclic voltammetry (CV) displays a progressively decreasing current density for the NaFSI:NMA=1.0:1.5 electrolyte over the first 10 cycles (Figure 4.6a-b), unlike the NaFSI:NMA=1.0:1.0 electrolyte. This suggests that its inferior passivation ability allows continuous reaction with Na, producing a progressively thicker interphase. The distribution of relaxation times (DRT) analysis of the EIS data supports this conclusion, showing an increased time constant for Na⁺ transport through the SEI compared to the 1.0:1.0 electrolyte (Figure 4.6c-d).[78, 101]

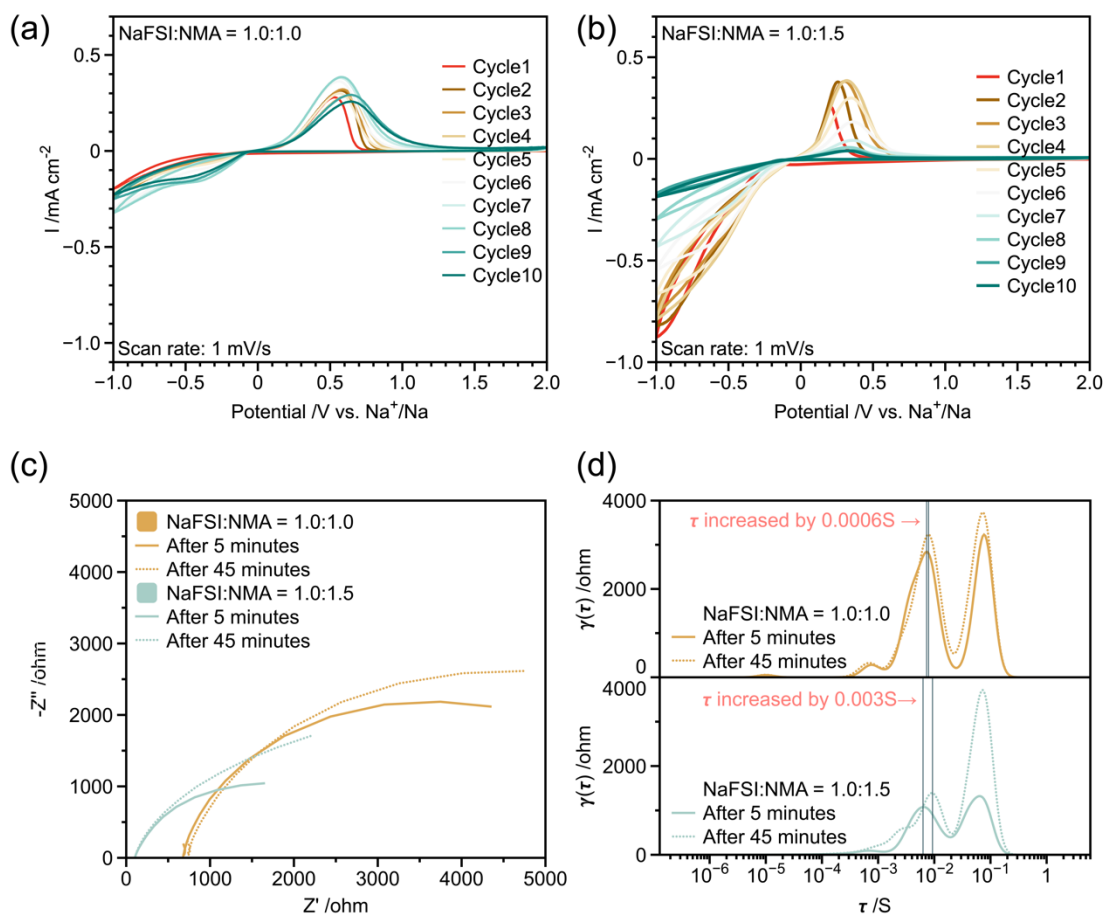


Figure 4.6: Cyclic voltammograms of Na//Cu for the first 10 cycles using electrolytes with NaFSI:NMA = 1.0:1.0 (a) and 1.0:1.5 (b); Electrochemical impedance spectroscopy (EIS) of Na//Cu cells: after 8 hour resting, 10 μ Ah of Na was plated onto Cu, followed by measuring EIS (c) after 5 and 45 minutes, and (d) the corresponding distribution of DRT analysis.

4.2 SEI dissolution

Organic SEIs, due to their polarity, have higher solubility, while inorganic SEIs remain stable and insoluble.[102-104] Any SEI dissolution is compensated by reformation, as evidenced by increased reduction capacity in subsequent cycles. Na//Cu cell data reveals substantial SEI dissolution in the less concentrated electrolyte, with far less dissolution observed in the more concentrated ones (Figure 4.7a-b), consistent with the XPS results.

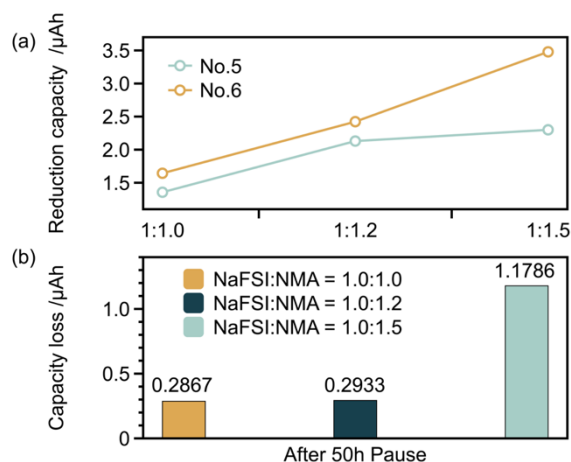


Figure 4.7: (a) Galvanostatic reduction capacity (at $3 \mu\text{A cm}^{-2}$) before and after the 50 hour pause, and (b) the corresponding capacity losses.

Moving to DRT analysis, for a pristine Cu metal surface at its open-circuit potential in contact with 1M NaPF₆ in EC:DMC electrolyte, the evidence (Figure 4.8a-b) points to little or no immediate decomposition as only the peak of charge-transfer is observed around 0.1 s. However, a SEI characteristic peak, corresponding to the high-frequency semicircle, appears in the τ range of 10^{-3} - 10^{-4} s when a fresh Na metal surface contacts this electrolyte (Figure 4.8c-d).

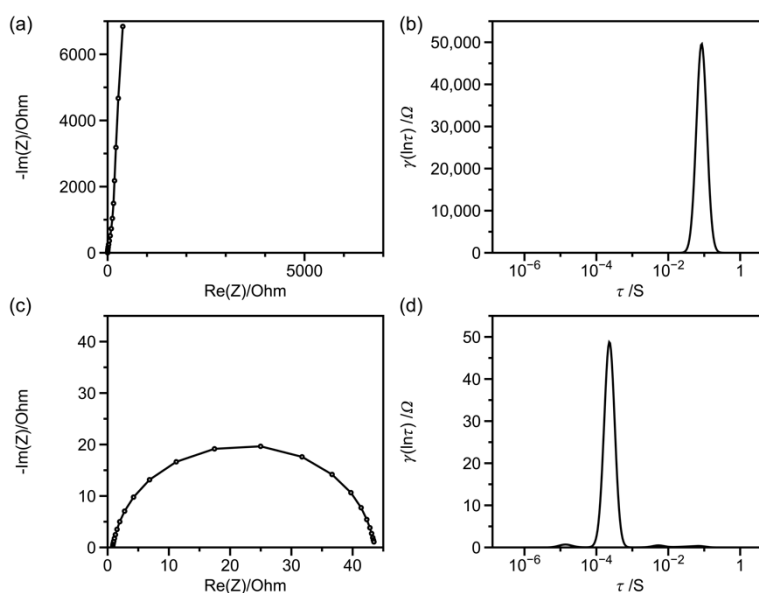


Figure 4.8: EIS curves after 8 h rest at room temperature with 1M NaPF₆ in EC:DMC electrolyte: (a) Na//Cu (Cu as WE), (b) its DRT spectrum; (c) Na//Na (Na as WE), (d) its DRT spectrum.

Sodium's SEI in carbonate is so unstable that a copper substrate will experience very low CE,[105] i.e., of the 2 mAh cm⁻² plated Na, most is consumed by SEI formation, leaving only a small amount of electrochemically active Na. Its full stripping occurs in only two cycles without reaching the 1V vs Na⁺/Na cutoff (Figure 4.9).

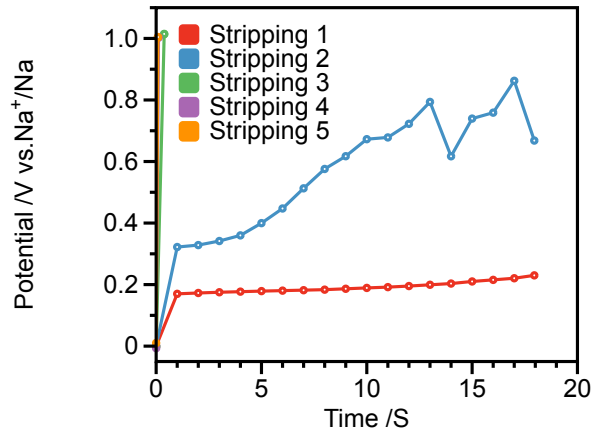


Figure 4.9: Stripping curves following 2 mAh cm⁻² Na plating, with 0.05 mAh cm⁻² per strip; ideal stripping lasts for 18 s at 10 mA cm⁻².

After the first stripping event, the SEI time constant τ decreases (Figure 4.10a-b), indicating that void formation induces SEI collapse and cracking, which increases porosity and Na⁺ permeability (faster ion transport). After the second strip, once electrochemically active Na is exhausted, τ remains unchanged, but the SEI resistance rises markedly. By equations 4-1 and 4-2, this resistance increase corresponds to a drop in capacitance C , reflecting a reduced SEI surface area. The same trend appears in Na//Na cells (Figure 4.10c-d), where the Na substrate fosters additional SEI growth in crack sites after plated Na depletion, causing τ to exceed its pre-stripping value.

$$\tau = R \times C \quad (4-1)[15]$$

Where τ (seconds) is the characteristic time constant, R (Ω) is the resistance of the process in question, and C (F) is its capacitance, i.e. the amount of charge the interface (double layer, surface film, etc.) can store.

$$C = \frac{\epsilon_r \epsilon_0 A}{d} \quad (4-2)[106]$$

Where C is the capacitance, ϵ_r is the relative permittivity, ϵ_0 is the vacuum permittivity, A is the plate area, and d is the distance between plates.

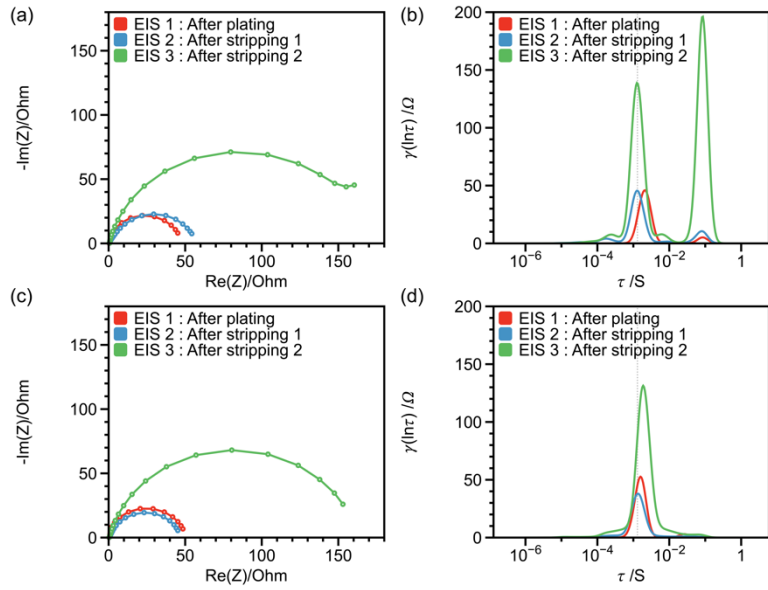


Figure 4.10: EIS curves after Na plating and stripping at room temperature with 1M NaPF₆ in EC:DMC electrolyte: (a) Na//Cu (Cu as WE), (b) its DRT spectra; (c) Na//Na (Na as WE), (d) its DRT spectra.

We developed a dual-cell configuration model (Figure 4.10) to semi-quantitatively characterize SEI dissolution during metal stripping. In both cell types, SEI evolution involves three concurrent processes: 1) Chemical dissolution of existing SEI; 2) Chemical repair, where cracks expose fresh Na to the electrolyte and regenerate SEI; 3) Mechanical loss, where void formation leads to localized SEI pitting.[107] In Na//Cu cells, once plated Na is exhausted, newly formed cracks can no longer be healed and therefore remain porous. In contrast, Na//Na cells retain an exposed Na substrate that continuously “heals” cracks by forming additional SEI, which manifests as an increased SEI resistance by comparing the post-stripping resistance of the two cells (i.e., R_6 - R_3 in Figure 4.11).

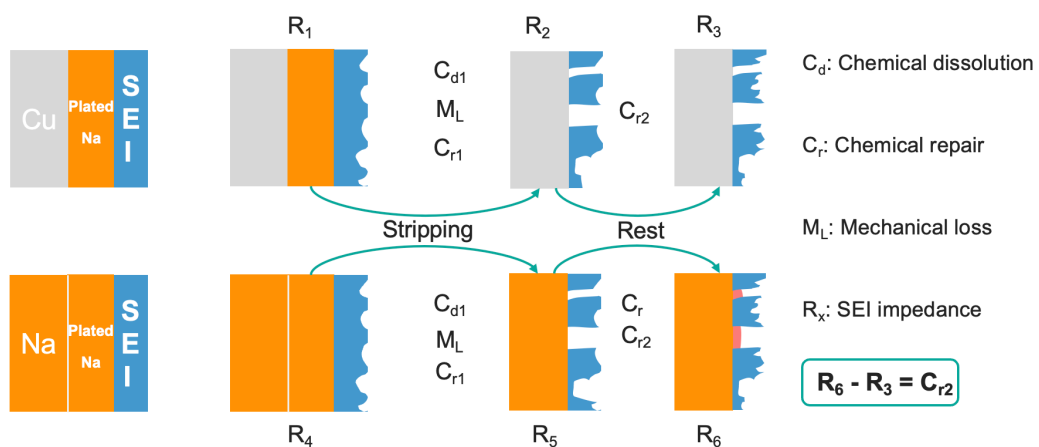


Figure 4.11: Schematic of dual-cell configuration model used for SEI dissolution analysis.

After the 2nd strip with electrochemically active Na depleted entirely, we found that the residual SEI on Na substrate is more resistive than that on Cu, showing larger time constants and higher resistance (ca. 143 Ω vs ca. 141 Ω) in Figure 4.12. Thus, the SEI dissolution due to Na stripping is semi-quantitatively estimated as 2 Ω .

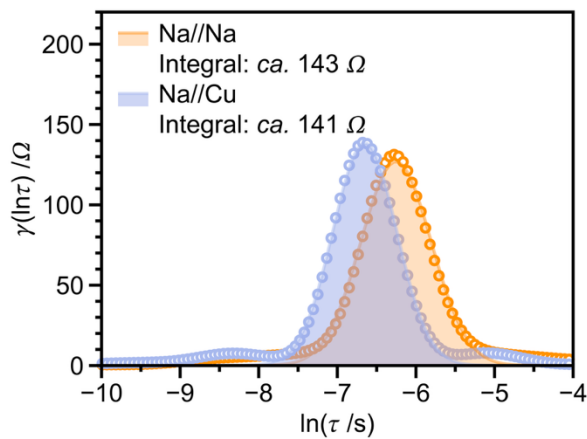


Figure 4.12: SEI peak fitting for DRT spectra of after the 2nd stripping event.

5 Conclusion and outlook

Our findings in paper I demonstrate that NMA indeed is a viable protic solvent for SMBs. The key is to minimize the concentration of free solvent at the Na interface and manage the proton dissociation, which collectively dictates the interfacial properties, e.g., by forming a more resistive/passivating SEI. Future work should focus on reducing electrolyte viscosity, as high salt concentration is necessary to address the reactivity of protic solvents with the Na anode. In Paper II, DRT analysis uncovers a quantitative increase in interfacial resistance after stripping, corresponding to SEI reformation at sites of void-induced cracking and partial dissolution, a degradation pathway that has been widely reported but rarely quantified. One can use DRT as a routine diagnostic to monitor the health of SEI and guide the design of electrolyte and interphase engineering towards SEIs with minimal resistance, negligible dissolution and maximal protection of Na metal surface. That said, small peaks in the DRT spectrum should be interpreted with care, as they can be spurious.

Acknowledgements

First and foremost, I would like to express my sincere gratitude to my supervisor, Patrik Johansson, for giving me the opportunity to do a PhD in the group and for providing me with the freedom to explore research topics that genuinely interest me. I have learned a lot from our discussions and manuscript revisions, particularly in terms of deep thinking and effective writing.

I am also deeply grateful to my co-supervisor, Julia Maibach, for her valuable insights on XPS and her support on the TEM proposal. A big thanks to my examiner, Aleksandar Matic, for his thought-provoking questions during our Monday meetings, as well as for all the jokes that made the PhD journey a little lighter.

A special thank you goes to Tomooki Hosaka for generously sharing his knowledge and for his patience during our discussions, always helping me to clear the fog whenever I encountered unsolved confusion.

I would also like to extend my warmest thanks to all past and present members of the Materials Physics division. Among them, I would like to thank Nguyen Ngoc Tan Luong for the MATLAB script and all our discussions on Raman spectroscopy. I am equally grateful to Patricia Huijbers for all the coordination job, which allowed us to focus on our research. Last but certainly not least, my sincere gratitude goes to Ezio Zanghellini, whose support has been invaluable in making the smooth progress of my research.

To my friends and family, I am truly thankful for your unwavering support, which has made me feel that I am not running forward alone.

Finally, I would like to acknowledge the financial support from the Swedish Research Council (VR) (grant #2021-00613).

Bibliography

- [1] A. Yao, S. M. Benson, W. C. Chueh, *Nat. Energy* **2025**, *10*, 404–416.
- [2] CATL, “CATL Unveils Freevov Super Hybrid Battery, Heralding a New Era of Sustainable Travel”, can be found under <https://www.catl.com/en/news/6301.html>, 2024 (accessed 20 February 2025).
- [3] J. Q. Zheng, C. H. Guan, H. X. Li, D. J. Wang, Y. Q. Lai, S. M. Li, J. Li, Z. Zhang, *Adv. Energy Mater.* **2024**, *14*, 2303584.
- [4] B. Sayahpour, W. K. Li, S. Bai, B. Y. Lu, B. Han, Y. T. Chen, G. Deysheer, S. Parab, P. Ridley, G. Raghavendran, L. H. B. Nguyen, M. H. Zhang, Y. S. Meng, *Energy Environ. Sci.* **2024**, *17*, 1216-1228.
- [5] Z. Huang, Z. Xiao, R. Jin, Z. Li, C. Shu, R. Shi, X. Wang, Z. Tang, W. Tang, Y. Wu, *Energy Environ. Sci.* **2024**, *17*, 5365-5386.
- [6] P. Wen, P. Lu, X. Shi, Y. Yao, H. Shi, H. Liu, Y. Yu, Z. S. Wu, *Adv. Energy Mater.* **2021**, *11*, 2002930.
- [7] Z. Wang, H. Zhang, J. Xu, A. Pan, F. Zhang, L. Wang, R. Han, J. Hu, M. Liu, X. Wu, *Adv. Funct. Mater.* **2022**, *32*, 2112598.
- [8] Y. Dong, P. Wen, H. Shi, Y. Yu, Z.-S. Wu, *Adv. Funct. Mater.* **2024**, *34*, 2213584.
- [9] P. Jankowski, K. Matuszek, M. Treskow, M. Armand, D. MacFarlane, P. Johansson, *Chem. Commun.* **2019**, *55*, 12523-12526.
- [10] A. Brandt, J. Pires, M. Anouti, A. Balducci, *Electrochim. Acta* **2013**, *108*, 226-231.
- [11] Z. Cheng, Z. Zhang, F. Qiu, Z. Gao, H. Xie, Z. Xu, M. Jia, X. Zhang, H. Zhou, *ACS Energy Lett.* **2024**, *10*, 177-184.
- [12] F. Huang, P. Xu, G. Fang, S. Liang, *Adv. Mater.* **2024**, *36*, 2405310.
- [13] D. De Sloovere, D. E. P. Vanpoucke, A. Paulus, B. Joos, L. Calvi, T. Vranken, G. Reekmans, P. Adriaensens, N. Eshraghi, A. Mahmoud, F. Boschini, M. Safari, M. K. Van Bael, A. Hardy, *Adv. Energy Sustain. Res.* **2022**, *3*, 2100159.
- [14] J. Lee, J. Kim, S. Kim, C. Jo, J. Lee, *Mater. Adv.* **2020**, *1*, 3143-3166.
- [15] Y. Lu, C.-Z. Zhao, J.-Q. Huang, Q. Zhang, *Joule* **2022**, *6*, 1172-1198.
- [16] M. Mandl, J. Becherer, D. Kramer, R. Mönig, T. Diemant, R. J. Behm, M. Hahn, O. Böse, M. A. Danzer, *Electrochim. Acta* **2020**, *354*, 136698.
- [17] J. K. Eckhardt, T. Fuchs, S. Burkhardt, P. J. Klar, J. Janek, C. Heiliger, *Adv. Mater. Interfaces* **2023**, *10*, 2202354.

- [18] X. Zheng, L. Huang, X. Ye, J. Zhang, F. Min, W. Luo, Y. Huang, *Chem* **2021**, *7*, 2312-2346.
- [19] P. Canepa, G. Sai Gautam, D. C. Hannah, R. Malik, M. Liu, K. G. Gallagher, K. A. Persson, G. Ceder, *Chem. Rev.* **2017**, *117*, 4287-4341.
- [20] C. Deng, X. Li, R. Chen, K. Ye, J. Lipton, S. A. Maclean, H. Wang, A. D. Taylor, G. M. Weng, *Energy Storage Mater.* **2023**, *60*, 102820.
- [21] H. Zhang, C. Li, G. G. Eshetu, S. Laruelle, S. Grugeon, K. Zaghbi, C. Julien, A. Mauger, D. Guyomard, T. Rojo, N. Gisbert-Trejo, S. Passerini, X. Huang, Z. Zhou, P. Johansson, M. Forsyth, *Angew. Chem. Int. Ed.* **2020**, *59*, 534-538.
- [22] C. Delmas, C. Fouassier, P. Hagemuller, *Physica B+ c* **1980**, *99*, 81-85.
- [23] K. Kubota, S. Komaba, *J. Electrochem. Soc.* **2015**, *162*, A2538.
- [24] S. P. Ong, V. L. Chevrier, G. Hautier, A. Jain, C. Moore, S. Kim, X. Ma, G. Ceder, *Energy Environ. Sci.* **2011**, *4*, 3680-3688.
- [25] Y. X. Wang, B. Zhang, W. Lai, Y. Xu, S. L. Chou, H. K. Liu, S. X. Dou, *Adv. Energy Mater.* **2017**, *7*, 1602829.
- [26] Y. Wang, D. Zhou, V. Palomares, D. Shanmukaraj, B. Sun, X. Tang, C. Wang, M. Armand, T. Rojo, G. Wang, *Energy Environ. Sci.* **2020**, *13*, 3848-3879.
- [27] J. Chen, Y. Peng, Y. Yin, M. Liu, Z. Fang, Y. Xie, B. Chen, Y. Cao, L. Xing, J. Huang, Y. Wang, X. Dong, Y. Xia, *Energy Environ. Sci.* **2022**, *15*, 3360-3368.
- [28] C. Bao, B. Wang, P. Liu, H. Wu, Y. Zhou, D. Wang, H. Liu, S. Dou, *Adv. Funct. Mater.* **2020**, *30*, 2004891.
- [29] B. Lee, E. Paek, D. Mitlin, S. W. Lee, *Chem. Rev.* **2019**, *119*, 5416-5460.
- [30] O. Borodin, J. Self, K. A. Persson, C. Wang, K. Xu, *Joule* **2020**, *4*, 69-100.
- [31] J. Tan, J. Liu, *Energy Environ. Mater.* **2021**, *4*, 302-306.
- [32] Q.-K. Zhang, X.-Q. Zhang, H. Yuan, J.-Q. Huang, *Small Sci.* **2021**, *1*, 2100058.
- [33] G. G. Eshetu, S. Grugeon, H. Kim, S. Jeong, L. Wu, G. Gachot, S. Laruelle, M. Armand, S. Passerini, *ChemSusChem* **2016**, *9*, 462-471.
- [34] A. Ponrouch, E. Marchante, M. Courty, J.-M. Tarascon, M. R. Palacin, *Energy Environ. Sci.* **2012**, *5*, 8572-8583.
- [35] M. Wang, Q. Wang, X. Ding, Y. Wang, Y. Xin, P. Singh, F. Wu, H. Gao, *Interdiscip. Mater.* **2022**, *1*, 373-395.
- [36] Z. Lin, Q. Xia, W. Wang, W. Li, S. Chou, *InfoMat* **2019**, *1*, 376-389.
- [37] Y. Li, F. Wu, Y. Li, M. Liu, X. Feng, Y. Bai, C. Wu, *Chem. Soc. Rev.* **2022**, *51*, 4484-4536.

- [38] J. Feng, L. Ci, S. Xiong, *RSC Adv.* **2015**, *5*, 96649-96652.
- [39] S. S. Zhang, *J. Power Sources* **2006**, *162*, 1379-1394.
- [40] H. Che, X. Yang, H. Wang, X.-Z. Liao, S. S. Zhang, C. Wang, Z.-F. Ma, *J. Power Sources* **2018**, *407*, 173-179.
- [41] M. Zhu, L. Li, Y. Zhang, K. Wu, F. Yu, Z. Huang, G. Wang, J. Li, L. Wen, H.-K. Liu, *Energy Storage Mater.* **2021**, *42*, 145-153.
- [42] G. Yan, K. Reeves, D. Foix, Z. Li, C. Cometto, S. Mariyappan, M. Salanne, J. M. Tarascon, *Adv. Energy Mater.* **2019**, *9*, 1901431.
- [43] J. Y. Jang, Y. Lee, Y. Kim, J. Lee, S.-M. Lee, K. T. Lee, N.-S. Choi, *J. Mater. Chem. A* **2015**, *3*, 8332-8338.
- [44] J. H. Kim, J. H. Hyun, S. Kim, W. H. Park, S. H. Yu, *Adv. Energy Mater.* **2025**, 2500587.
- [45] B. Mosallanejad, S. S. Malek, M. Ershadi, A. A. Daryakenari, Q. Cao, F. B. Ajdari, S. Ramakrishna, *J. Electroanal. Chem.* **2021**, *895*, 115505.
- [46] X. Cao, H. Jia, W. Xu, J.-G. Zhang, *J. Electrochem. Soc.* **2021**, *168*, 010522.
- [47] J. Lee, Y. Lee, J. Lee, S.-M. Lee, J.-H. Choi, H. Kim, M.-S. Kwon, K. Kang, K. T. Lee, N.-S. Choi, *ACS Appl. Mater. Interfaces* **2017**, *9*, 3723-3732.
- [48] J. Wang, Y. Yamada, K. Sodeyama, E. Watanabe, K. Takada, Y. Tateyama, A. Yamada, *Nat. Energy* **2018**, *3*, 22-29.
- [49] K. Takada, Y. Yamada, E. Watanabe, J. Wang, K. Sodeyama, Y. Tateyama, K. Hirata, T. Kawase, A. Yamada, *ACS Appl. Mater. Interfaces* **2017**, *9*, 33802-33809.
- [50] R. Cao, K. Mishra, X. Li, J. Qian, M. H. Engelhard, M. E. Bowden, K. S. Han, K. T. Mueller, W. A. Henderson, J.-G. Zhang, *Nano Energy* **2016**, *30*, 825-830.
- [51] M. He, K. C. Lau, X. Ren, N. Xiao, W. D. McCulloch, L. A. Curtiss, Y. Wu, *Angew. Chem. Int. Ed.* **2016**, *55*, 15310-15314.
- [52] Y. Wang, R. Jiang, Y. Liu, H. Zheng, W. Fang, X. Liang, Y. Sun, R. Zhou, H. Xiang, *ACS Appl. Energy Mater.* **2021**, *4*, 7376-7384.
- [53] Y. Li, Y. Yang, Y. Lu, Q. Zhou, X. Qi, Q. Meng, X. Rong, L. Chen, Y.-S. Hu, *ACS Energy Lett.* **2020**, *5*, 1156-1158.
- [54] L. O. S. Colbin, R. Mogensen, A. Buckel, Y. L. Wang, A. J. Naylor, J. Kullgren, R. Younesi, *Adv. Mater. Interfaces* **2021**, *8*, 2101135.
- [55] R. Mogensen, S. Colbin, A. S. Menon, E. Björklund, R. Younesi, *ACS Appl. Energy Mater.* **2020**, *3*, 4974-4982.
- [56] O. Borodin, G. Smith, *J. Solution Chem.* **2007**, *36*, 803-813.

- [57] T. P. Liyana-Arachchi, J. B. Haskins, C. M. Burke, K. M. Diederichsen, B. D. McCloskey, J. W. Lawson, *J. Phys. Chem. B* **2018**, *122*, 8548-8559.
- [58] M. Okoshi, C.-P. Chou, H. Nakai, *J. Phys. Chem. B* **2018**, *122*, 2600-2609.
- [59] O. Borodin, L. Suo, M. Gobet, X. Ren, F. Wang, A. Faraone, J. Peng, M. Olguin, M. Schroeder, M. S. Ding, E. Gobrogge, A. von Wald Cresce, S. Munoz, J. A. Dura, S. Greenbaum, C. Wang, K. Xu, *ACS Nano* **2017**, *11*, 10462-10471.
- [60] J. Hu, Y. Ji, G. Zheng, W. Huang, Y. Lin, L. Yang, F. Pan, *Aggregate* **2022**, *3*, e153.
- [61] R. Andersson, F. Årén, A. A. Franco, P. Johansson, *J. Electrochem. Soc.* **2020**, *167*, 140537.
- [62] C. Zhang, K. Ueno, A. Yamazaki, K. Yoshida, H. Moon, T. Mandai, Y. Umebayashi, K. Dokko, M. Watanabe, *J. Phys. Chem. B* **2014**, *118*, 5144-5153.
- [63] D. W. McOwen, D. M. Seo, O. Borodin, J. Vatamanu, P. D. Boyle, W. A. Henderson, *Energy Environ. Sci.* **2014**, *7*, 416-426.
- [64] M. Gauthier, T. J. Carney, A. Grimaud, L. Giordano, N. Pour, H.-H. Chang, D. P. Fenning, S. F. Lux, O. Paschos, C. Bauer, F. Maglia, S. Lupart, P. Lamp, Y. Shao-Horn, *J. Phys. Chem. Lett.* **2015**, *6*, 4653-4672.
- [65] Y. You, A. Manthiram, *Adv. Energy Mater.* **2018**, *8*, 1701785.
- [66] C. Yan, R. Xu, Y. Xiao, J.-F. Ding, L. Xu, B.-Q. Li, J.-Q. Huang, *Adv. Funct. Mater.* **2020**, *30*, 1909887.
- [67] Y. Yamada, J. Wang, S. Ko, E. Watanabe, A. Yamada, *Nat. Energy* **2019**, *4*, 269-280.
- [68] L. Lutz, D. Alves Dalla Corte, M. Tang, E. Salager, M. Deschamps, A. Grimaud, L. Johnson, P. G. Bruce, J.-M. Tarascon, *Chem. Mater.* **2017**, *29*, 6066-6075.
- [69] S. Shi, P. Lu, Z. Liu, Y. Qi, L. G. Hector, Jr., H. Li, S. J. Harris, *Journal of the American Chemical Society* **2012**, *134*, 15476-15487.
- [70] Q. Zhang, J. Pan, P. Lu, Z. Liu, M. W. Verbrugge, B. W. Sheldon, Y.-T. Cheng, Y. Qi, X. Xiao, *Nano Lett.* **2016**, *16*, 2011-2016.
- [71] L. D. S. Yadav, *Organic spectroscopy*, Springer Science & Business Media, **2004**.
- [72] W. Zheng, *Chemistry-Methods* **2023**, *3*, e202200042.
- [73] D. L. Pavia, G. M. Lampman, G. S. Kriz, J. R. Vyvyan, *Introduction to spectroscopy*, **2015**.
- [74] I. Källquist, R. Le Ruyet, H. Liu, R. Mogensen, M.-T. Lee, K. Edström, A. J. Naylor, *J. Mater. Chem. A* **2022**, *10*, 19466-19505.
- [75] J. Chastain, R. C. King Jr, *Perkin-Elmer Corporation* **1992**, *40*, 25.

- [76] A. J. Bard, L. R. Faulkner, H. S. White, *Electrochemical methods: fundamentals and applications*, John Wiley & Sons, **2022**.
- [77] T. H. Wan, M. Saccoccio, C. Chen, F. Ciucci, *Electrochim. Acta* **2015**, *184*, 483-499.
- [78] A. Maradesa, B. Py, T. H. Wan, M. B. Effat, F. Ciucci, *J. Electrochem. Soc.* **2023**, *170*, 030502.
- [79] X. Tan, M. Chen, J. Zhang, S. Li, H. Zhang, L. Yang, T. Sun, X. Qian, G. Feng, *Adv. Energy Mater.* **2024**, *14*, 2400564.
- [80] E. Lindahl, B. Hess, D. Van Der Spoel, *Mol. Model. Annu.* **2001**, *7*, 306-317.
- [81] W. L. Jorgensen, J. Tirado-Rives, *Proc. Natl. Acad. Sci.* **2005**, *102*, 6665-6670.
- [82] L. S. Dodda, I. Cabeza de Vaca, J. Tirado-Rives, W. L. Jorgensen, *Nucleic Acids Res.* **2017**, *45*, W331-W336.
- [83] L. Martínez, R. Andrade, E. G. Birgin, J. M. Martínez, *J. Comput. Chem.* **2009**, *30*, 2157-2164.
- [84] J. Timhagen, C. Cruz, J. Weidow, P. Johansson, *Batter. Supercaps.* **2024**, *7*, e202400297.
- [85] R. Kumar, J. Schmidt, J. Skinner, *J. Chem. Phys.* **2007**, *126*, 204107.
- [86] A. Kottarathil, Z. Slim, H. A. Ishfaq, S. Jeschke, G. Z. Żukowska, M. Marczewski, K. Lech, P. Johansson, W. Wieczorek, *J. Electrochem. Soc.* **2024**, *171*, 070506.
- [87] T. Shi, R. Hou, L. Zheng, H. Lu, C. Xu, X. Sun, P. He, S. Li, H. Zhou, S. Guo, *Adv. Energy Mater.*, 2405803.
- [88] X.-B. Chen, W.-H. Fang, D.-C. Fang, *Journal of the American Chemical Society* **2003**, *125*, 9689-9698.
- [89] A. Al-Khalili, R. Thomas, A. Ehlerding, F. Hellberg, W. Geppert, V. Zhaunerchyk, M. af Ugglas, M. Larsson, E. Uggerud, J. Vedde, *J. Chem. Phys.* **2004**, *121*, 5700-5708.
- [90] J. Li, S. Qin, M. Xu, W. Wang, J. Zou, Y. Zhang, H. Dou, Z. Chen, *Adv. Funct. Mater.* **2024**, *34*, 2402186.
- [91] N. Z. Hardin, Z. Duca, A. Imel, P. A. Ward, *ChemElectroChem* **2022**, *9*, e202200628.
- [92] I. V. Rubtsov, K. Kumar, R. M. Hochstrasser, *Chem. Phys. Lett.* **2005**, *402*, 439-443.
- [93] L. Geng, X. Wang, K. Han, P. Hu, L. Zhou, Y. Zhao, W. Luo, L. Mai, *ACS Energy Lett.* **2022**, *7*, 247-260.
- [94] B. Aktekin, L. M. Riegger, S.-K. Otto, T. Fuchs, A. Henss, J. Janek, *Nat. Commun.* **2023**, *14*, 6946.
- [95] J. Li, S. Sui, X. Zhou, K. Lei, Q. Yang, S. Chu, L. Li, Y. Zhao, M. Gu, S. Chou, *Angew. Chem. Int. Ed.* **2024**, *63*, e202400406.

- [96] V. Nefedov, Y. V. Salyn, G. Leonhardt, R. Scheibe, *J. Electron. Spectrosc. Relat. Phenom.* **1977**, *10*, 121-124.
- [97] P. Citrin, *Phys. Rev. B* **1973**, *8*, 5545.
- [98] Y. He, P. Zou, S.-M. Bak, C. Wang, R. Zhang, L. Yao, Y. Du, E. Hu, R. Lin, H. L. Xin, *ACS Energy Lett.* **2022**, *7*, 2866-2875.
- [99] C. Huang, X. Zhao, Y. Hao, Y. Yang, Y. Qian, G. Chang, Y. Zhang, Q. Tang, A. Hu, X. Chen, *Small* **2022**, *18*, 2203674.
- [100] L.-L. Jiang, C. Yan, Y.-X. Yao, W. Cai, J.-Q. Huang, Q. Zhang, *Angew. Chem. Int. Ed.* **2021**, *60*, 3402-3406.
- [101] A. Maradesa, B. Py, J. Huang, Y. Lu, P. Iurilli, A. Mrozinski, H. M. Law, Y. Wang, Z. Wang, J. Li, *Joule* **2024**, *8*, 1958-1981.
- [102] L. A. Ma, A. J. Naylor, L. Nyholm, R. Younesi, *Angew. Chem. Int. Ed.* **2021**, *60*, 4855-4863.
- [103] Y. Ji, J. Qiu, W. Zhao, T. Liu, Z. Dong, K. Yang, G. Zheng, G. Qian, M. Yang, Q. Chen, *Chem* **2023**, *9*, 2943-2955.
- [104] X. Liu, X. Zheng, Y. Dai, B. Li, J. Wen, T. Zhao, W. Luo, *Adv. Mater.* **2023**, *35*, 2304256.
- [105] B. Sayahpour, W. Li, S. Bai, B. Lu, B. Han, Y.-T. Chen, G. Deyscher, S. Parab, P. Ridley, G. Raghavendran, L. H. B. Nguyen, M. Zhang, Y. S. Meng, *Energy Environ. Sci.* **2024**, *17*, 1216-1228.
- [106] P. Simon, Y. Gogotsi, *Nat. Mater.* **2008**, *7*, 845-854.
- [107] F. Shi, A. Pei, D. T. Boyle, J. Xie, X. Yu, X. Zhang, Y. Cui, *Proc. Natl. Acad. Sci.* **2018**, *115*, 8529-8534.